Hydrochromic Full-Color MXene Quantum Dots through Hydrogen Bonding toward Ultrahigh-Efficiency White Light-Emitting Diodes

Quan Xu[†*], Wenjing Yang[†], Yangyang Wen[†], Shengkun Liu[†], Zheng Liu[§], Wee-Jun Ong[‖#*], and Neng Li[‡*]

† State Key Laboratory of Heavy Oil Processing, Harvard SEAS-CUPB Joint Laboratory on Petroleum Science, China University of Petroleum-Beijing, 102249, China. E-mail: xuquan@cup.edu.cn

‡ State Key Laboratory of Silicate Materials for Architectures, Wuhan University of Technology, 430070, China. E-mail: lineng@whut.edu.cn

§ Centre for Programmable Materials, School of Materials Science and Engineering, Nanyang Technological University, 50 Nanyang Avenue, Singapore 637371, Singapore

‖ School of Energy and Chemical Engineering, Xiamen University Malaysia, Selangor Darul Ehsan 43900, Malaysia. E-mail: weejun.ong@xmu.edu.my;

College of Chemistry and Chemical Engineering, Xiamen University, Xiamen 361005, China

ABSTRACT: Multiple-color emissive MXene quantum dots (MQDs) exhibit vast application prospects in various fields, including optoelectronics, bioimaging, and catalysis. However, the majority of the recent MQDs display limited maximum emission in the blue-light region. Herein, we employ the hydrogen bonds as an adjustment method to prepare novel full-color MQDs using Ti_3C_2 MXene as the starting material. By doping with sodium thiosulfate and ammonia water (sulfur-doped, nitrogen-doped), the maximum emission of the obtained MQDs demonstrates entire light spectrum covering from blue to orange light. Interestingly, the as-synthesized Ti_3C_2 MQDs aqueous solutions unveil multiple-color, excitation-independent emission wavelength and fluorescence (lifetime and quantum yield) enhancement compared with in the dry state. The fluorescence shift and enhancement are confirmed by comprehensive spectroscopic techniques (e.g. grazing incidence X-ray diffraction (GIXRD)) and complementary density functional theory (DFT) calculations. The results indicate that the construction of stalwart bridge-like hydrogen-bonded networks between the MQDs by highly ordered bound water on the doped MQDs surface can give rise to the immobilization of the C=O and C-O bonds of the MQDs, thus strengthening the rigidity of the entire system. As a benefit of the bandgap emission, white light-emitting diodes (WLEDs) with stable emission color by directly utilizing MQDs as an active emission layer have been realized for the first time. As such, the as-prepared full-color MQDs developed herein can remarkably broaden the prospect of MXene 2D quantum dots (2D-QDs) in a myriad of technological applications such as electronics, batteries, bioimaging, and cancer therapy.

KEYWORDS: MXene quantum dots, multiple color, hydrochromic, hydrogen bond, white light-emitting diodes

Introduction

To date, the great success of graphene materials has triggered tremendous enthusiasm for exploring novel two-dimensional (2D) layered inorganic materials[1] such as hexagonal boron nitride (*h*-BN),[2,3] transition metal dichalcogenides (TMDs),[4,5] graphitic carbon nitride (g-C_3N_4),[6-8] monoatomic buckled crystals,[9,10] bis(dipyrrinato)zinc(II) complex nanosheet,[11,12] to meet new application requirements.[13-18] When these bulk 2D materials are converted into zero-dimensional (0D) forms (i.e. lateral dimensions generally smaller than 100 nm, typically <10 nm), eminent edge and strong quantum confinement effects can render intriguing properties, and some intrinsic virtue of the original 2D materials can be conserved at the same time. [19,20] The new family of 0D materials (2D-QDs) is endowed with ameliorated physico-chemical properties compared with the 2D parents, including improved dispersibility in both aqueous and non-aqueous media, easier functionalization or doping, and more novel luminescence.[19-21] The unique and diverse properties of 2D-QDs make them applicable in various fields such as bioimaging,[22-26] cancer therapy,[27,28] sensing,[29-31] optoelectronics,[32,33] catalysis,[34,35] supercapacitors,[36,37] energy storage[38,39] and batteries.[40,41]

In recent years, quantum dots (QDs) derived from 2D inorganic MXene materials (first introduced by Barsoum's group in 2011[42]), have begun to attract considerable attention, but still belong to a nascent research domain at present (Some reported two-dimensional quantum dots[43,44] are presented in Table S1). MXenes have demonstrated greet metallic conductivity and hydrophilicity,[45] but the low photoluminescence (PL) response in aqueous solution significantly limits their direct use in the field of bioimaging and optoelectronics.[46-48] In our previous work, we have successfully fabricated the nitrogen-doped MXene QDs with a remarkably high quantum yield (QY) of up to 18% with blue spectral.[49] However, there is a paucity of reports on the green-to-red emission MXene dots in order to bring MXene QDs into practical applications such as full-color displays, LEDs, optoelectronic devices, and photothermal therapy. Thus, a new strategy of engineering high efficiency full color MXene QDs dictates a necessity for practical implementation. What's more, the unique traits of 2D MXene QDs can substantially broaden the potential technological applications of 2D-QDs materials.

Herein, by using the hydrogen bonding as an adjustment controllable strategy, we have successfully prepared full-color MXene QDs with QYs up to 28.12%, 8.33% and 7.78%. In this work, we reported the synthesis of

hydrochromic MQDs in blue, yellow and orange using layered Ti_3C_2 as a precursor. The prepared MQDs contained sulfur-doped MQDs (S-MQDs), nitrogen-doped MQDs (N-MQDs) as well as sulfur and nitrogen co-doped MQDs (SN-MQDs), and exhibited an excitation-independent PL spectrum, full-color fluorescence and fluorescence (lifetime and QY) enhancement due to the construction of stalwart bridge-like hydrogen-bonded networks between the MQDs by highly ordered bound water on the doped MQDs surface. This can give rise to the immobilization of the C=O and C-O bonds of the MQDs and rigidity of the entire system. Moreover, the increasing lateral size because of the bridge-like hydrogen-bond caused the decline of the band gap stemming from π-electron delocalization. Furthermore, WLEDs were realized by using these doped MQDs. White-color emitting MQDs (W-MQDs) composites were covered on commercial UV emissive chips, and the WLEDs were fabricated based on the pure W-MQDs composite materials, with Commission Internationale de L'Eclairage (CIE) of (0.31, 0.35) and stable photoluminescence properties. As such, the synthesized MQDs have vast potential to be used as a fluorescent coating in WLED technology.

Results and Discussion

The synthesis scheme of the MQDs is shown in Figure 1a. Scanning electron microscopy (SEM), transmission electron microscope (TEM) and high resolution TEM (HRTEM) images of the Ti_3C_2 powders obtained after HF etching are shown in Figure S1 and Figure 1b. The results demonstrated the successful removal of the Al layer from Ti_3AlC_2, leading to the formation of layered Ti_3C_2 nanosheets, similar to the production of graphene using graphite exfoliation. The UV-vis absorption and PL spectra of the obtained MQDs under 360 nm UV irradiation are presented in Figure 1c-e. The spectra exemplified a strong absorption peak at 300 nm, corresponding to the n-π* transition, and another absorbance peak was discovered at 240 nm, indicative of the π-π* transition. The PL spectra of the obtained MQDs are exhibited in Figure 1f-h. The maximum PL emission values of SN-MQDs and N-MQDs are 572 and 525 nm, which is corresponded to the orange and yellow light, respectively. Interestingly, the S-MQDs displayed excitation-dependent emission wavelength and a blue fluorescence. Moreover, the PL quantum yield (QY, Table S2) of the MQDs was investigated by a comparative method, which recorded 28.12%, 8.33% and 7.78% for SN-MQDs, N-MQDs, and S-MQDs, respectively. The PL decays of SN-MQDs, N-MQDs and S-MQDs are fitted with multi-exponential function and the calculated lifetimes of MQDs are determined to be 7.74, 5.81 and 4.67 ns, respectively (Table S3). The photostability of these obtained MQDs was investigated (Figure S2). The PL

spectra of all prepared MQDs were highly stable with no identifiable changes in UV-vis absorption and photoluminescence intensities over different durations. The results can be ascribed to the adequate surface passivation of the SN-MQDs, S-MQDs and N-MQDs. Moreover, there was no evident decrease in the fluorescence at different pH values (Figure S3) either, signifying a wide range of potential applications of the as-synthesized MQDs.

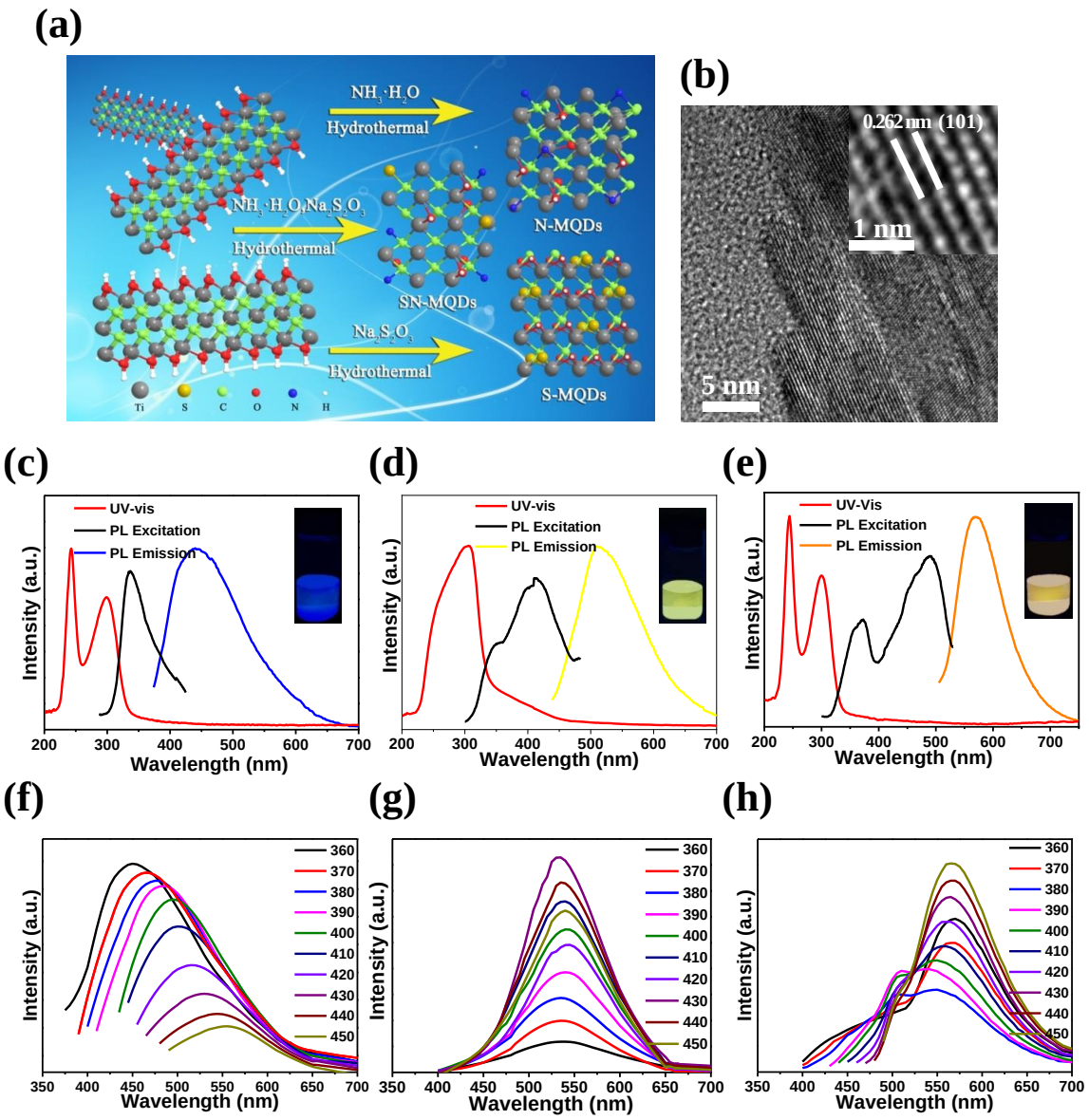

Figure 1. (a) Schematic of the synthesis of S-MQDs, N-MQDs and SN-MQDs. (b) HRTEM image of pristine Ti_3C_2. Inset (top-right): Enlarged view of the HRTEM image. UV-vis absorption spectra and PL spectra (excitation and emission scans) under 360 nm UV irradiation of (c) S-MQDs, (d) N-MQDs and (e) SN-MQDs. Inset (top-right): Photographs of MQDs under

365 nm UV irradiation. Fluorescent emission spectra of the (f) S-MQDs, (g) N-MQDs and (h) SN-MQDs at different excitation wavelengths.

In previous studies, due to the large heterogeneity in the synthesis, the luminescence mechanism of QDs is governed by numerous parameters such as size, edge configuration, shape, functional groups, defects and heterogeneous hybridization of the carbon network.[50] The PL mechanisms of the synthesized MQDs were studied and possible molecular interactions and light-emitting mechanism in water solution are illustrated in Figure 2a. The doped Ti_3C_2 connected with each other via hydrogen bonds with water molecules, resulting in the increase of lateral size of QDs (Figure 2b). The decline of the band gap owing to π-electron delocalization led to the red-shift of the emissive spectra when the lateral size was increased.[51] Dynamic light scattering (DLS) size distributions are shown in Figure 2c. Due to the construction of stalwart bridge-like hydrogen-bonded networks between the MQDs, the mean diameters of sulfur and nitrogen co-doped Ti_3C_2 hydrogen-bonded network and nitrogen doped Ti_3C_2 hydrogen-bonded network are 123.9 and 101.7 nm, respectively. S-MQDs has no particle size distribution of more than 20 nm except TiO_2 in the pattern, indicating that S-MQDs does not form a hydrogen-bonded network. TiO_2 with an average particle size of about 500 nm appeared in all QDs. Apart from that, MQDs in the dry state had a unique and strong emission centered at ca. 440 nm (Figure S4a-c). When the MQDs were excited at wavelengths in the range of 320 and 380 nm, the fluorescence main peak remained at 440 nm and the fluorescence intensity was apparently unchanged. However, when the dry MQDs were redispersed in the aqueous solution (Figure S4d-f), the multi-color fluorescence could be restored and was relatively stable with only a small amount of blue shift (~10 nm). Interestingly, this fluorescence recovery phenomenon does not exist in other solvents (Figure S4i).

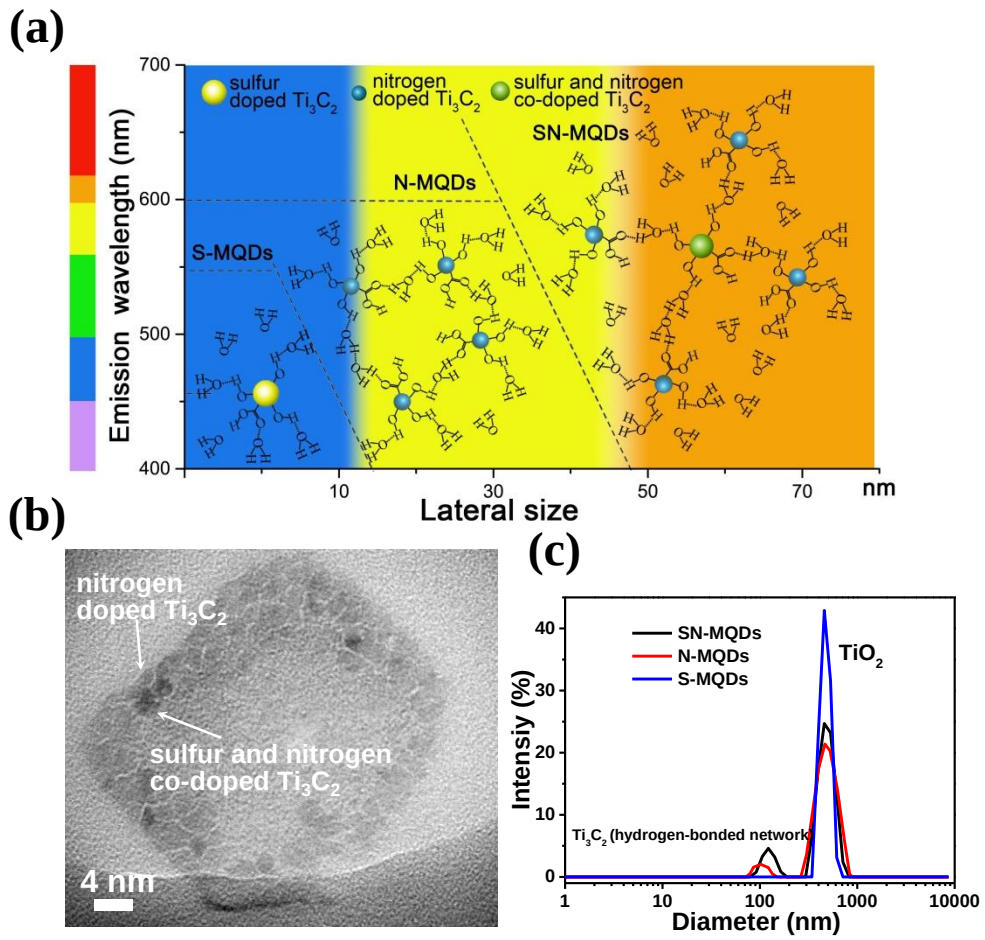

Figure 2. (a) Schematic of the molecular interactions and light-emitting mechanism of MQDs in the water solution. (b) The corresponding HRTEM image of SN-MQDs in relation to the mechanism. (c) Dynamic light scattering (DLS) size distributions of the synthesized MQDs in deionized water.

To comprehend the effect of water molecule on PL mechanism of MQDs, it is noteworthy that the fluorescence was not linearly related to the water content. An obvious emission shift and broaden were observed for more than 50% water content (Figure 3a-c). In Figure 3d-e, typical Raman peaks of various water contents of SN-MQDs at 1052 and 1648 cm^{-1} were observed,[52,53] corresponding to C-O and C=O stretching, respectively. As the contents of water increased from 0% to 80%, the C-O peak presented a blue shift from 1052 to 1061 cm^{-1}, whereas the C=O peak displayed a red shift from 1648 to 1637 cm^{-1}. This clearly indicated that both C-O and C=O of the SN-MQDs had a strong hydrogen bond interaction with water molecules,[52,54] causing doped Ti_3C_2 being interconnected by water molecules (Figure 2a).

To further unravel the effect of the hydrogen bonding, we employ ethanol as a widely used organic solvent, which is prone to form hydrogen bonding facilely and also as a solvent to redisperse the dry MQDs. The dry S-

MQDs possess negligible luminescence intensity in ethanol for the poor solubility, while the fluorescence spectra of SN-MQDs (ethanol) and N-MQDs (ethanol) reveal a slight blue shift compared with the dry state (Figure S4g-h). By comparing with the dry state, the differences imply the influence with hydroxyl by solvents, and it is apparent that forming hydrogen bonds is inadequate to cause size changes and fluorescence shifts.

There are three types of water existing in the vicinity of the matrix: bulk water, freezing bound water, and non-freezing bound water. In particular, bound water exhibits distinctive structural properties in comparison with bulk water, for instance, difficulty in freezing, difficult separation, and restricted mobility and solubility, which endow it with unique applications.[55-57] The lifetimes and photoluminescence QY of synthesized MQDs and dispersed MQDs were investigated (Figure 3f-g) with the fitted parameters shown in Tables S2 and S3. The lifetimes and QY of synthesized and dispersed MQDs (water) reveal a strong enhancement relative to the dry state, especially SN-MQDs (2.88 nm and 3.84% to 7.74 nm and 28.12%), while dispersing MQDs in alcohol seems few effects. The reason of fluorescence enhancement is the fabrication of stalwart bridge-like hydrogen-bonded networks between the Ti_3C_2 particles by highly ordered bound water on the doped MQDs surface, leading to the immobilization of the C=O and C-O bonds of the MQDs, thus vastly strengthening the rigidity of the entire system.[53] The use of bound water to achieve fluorescence shift and fluorescence enhancement acts as a significant role in biological applications such as cell imaging and disease diagnosis because of the extensive presence of bound water in cells and biological tissues.

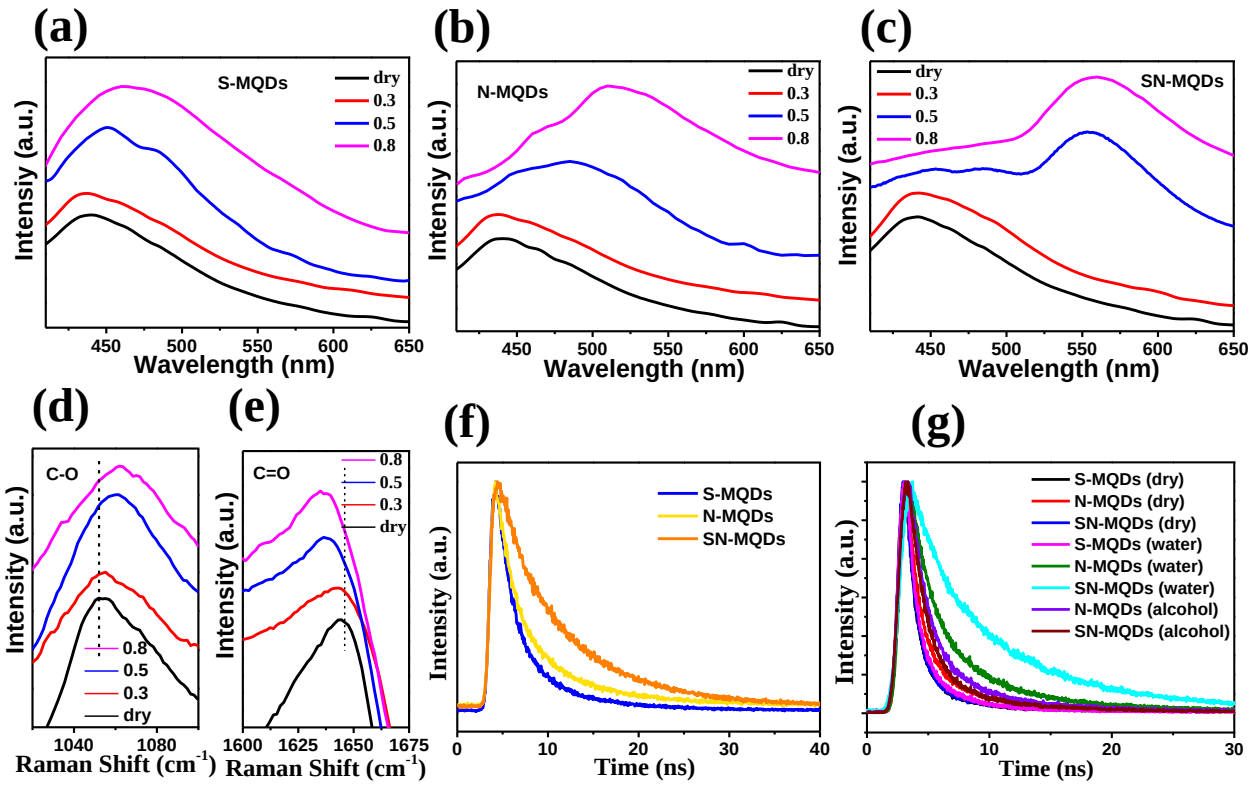

Figure 3. Different water content spectra (UV irradiation at 370 nm) of (a) S-MQDs, (b) N-MQDs and (c) SN-MQDs. Raman spectra of (d) C-O and (e) C=O bands of SN-MQDs in different water contents. (f-g) PL decay spectra of the as-synthesized MQDs, dry and redispersed MQDs.

The phase composition of the obtained MQDs and pristine Ti_3C_2 was investigated via XRD. As shown in Figure 4a, the pattern of the HF etched Ti_3C_2 nanoplatelets exhibited distinct (002) and (004) peaks, conformed to the previous XRD studies.[42,58] This result shows that the obtained Ti_3C_2 has a 2D layered structure, consistent with the SEM and HRTEM images (Figures S1 and 1b). The patterns of the synthesized SN-MQDs, N-MQDs and S-MQDs have the same characteristic peaks of (002) and (004), unambiguously demonstrating that the 2D layered structure is preserved after the hydrothermal reaction. A peak at 34.0° of MQDs is observed, corresponding to (101) peak, which is in accordance with the HRTEM images (Figure 5d-f). Figure 4b illustrates the normalized grazing incidence XRD (GIXRD) patterns of MQDs and pristine Ti_3C_2. The (002) peak of the synthesized materials exemplified a slight shift to a lower angle compared to the pristine Ti_3C_2 (8.8°) due to the heterogeneous element doping, indicating a slight broadening in the d-spacing from 1.01 to 1.09 nm (△d-spacing: ~0.08 nm).

The bonding configurations in the C1*s*, N1*s*, S2*p* and Ti2*p* region for MQDs and pristine Ti_3C_2 were determined by X-ray photoelectron spectroscopy (XPS) (Figures 4c-f and S5). Four peaks at 281.5, 284.8, 286.2 and 288.6 eV

were found in the C1*s* XPS spectrum of Ti_3C_2, representing the C−Ti, C−C/C−H, C−O and C=O bonds, respectively.[59] The C1*s* XPS spectrum of S-MQDs exhibits a peak at 285.57 eV, which is assigned to the C-S bonding configuration. As for N-MQDs, two peaks were emerged, corresponding to the C=N bond (286.1 eV) and C-N bond (287.5 eV), highlighting that doped atoms and carbon atoms formed chemical bonds after the Ti_3C_2 underwent hydrothermal treatment. Compared with S-MQDs and N-MQDs, the C1*s* XPS spectrum of SN-MQDs (Figure S4b) exhibited the formation of C-S bonds as well as C-N/C=N bonds. As such, this confirms the successful co-doping of N and S into the Ti_3C_2 nanosheet. The formation of C-N/C=N bonds was more dominant when the SN-MQDs were heterogeneous element doped, manifesting that the formation of C-N/C=N was relatively easier to overcome the energy barrier than the C-S bonds.

High-resolution N1*s* spectra were utilized to analyze the nature of chemical bonding of nitrogen atoms in pristine Ti_3C_2, N-MQDs and SN-MQDs. The pristine Ti_3C_2 and S-MQDs basically showed no signal. However, three new peaks situated at 396.07, 399.5 and 401.2 eV were obtained by peak fitting, which can be assigned to the Ti-N band, pyrrole-like nitrogen (C=N), and "graphitic" nitrogen (C-N), respectively.[60] Carbon sites with a larger shrinkage of the defect-induced bond were more likely originated from the N doping when a pyrrole-like nitrogen was produced, and if present, N-doping also exists at the apex of the pentagonal ring.[61] Besides, there was no distinct difference between the patterns of SN-MQDs and N-MQDs, revealing that the presence of sulfur doping has no influence on the formation of nitrogen doping.

The S2*p* XPS spectra of S-MQDs (Figure 4e) were fitted by two peaks located at 162.47 and 168.2 eV. Two different components were found in the former peak, in which one of them at 161.87 eV was assigned to the 2*p*3/2 positions of TiOS, a new type of titanium oxysulfides due to the fact that S^{2-} could not be associated with titanium atoms in the TiS_2 environment.[62] The other peak at 163.5 eV was accredited to the 2*p*3/2 sites of thiophene-S (C-S-C) due to their spin orbit coupling.[63] On the other hand, three components at 167.6, 168.5 and 169.3 eV were acquired by peak fitting in the latter peak, related to different oxidized sulfur form of SO_x (x = 2–4) bond, generally linked on the surface of the Ti_3C_2 layers. However, the S2*p* XPS spectra of SN-MQDs showed a small peak at 160.97 eV, corresponding to the Ti-S band of TiS_2.

The spectra of Ti 2*p* (Figure 4f) depicted four doublets (Ti $2p_{3/2}$−Ti $2p_{1/2}$).[64] The Ti $2p_{3/2}$ components of Ti−C bond and Ti^{4+} (TiO_2) were centred at 454.9 and 458.5 eV, respectively.[65,66] Not only that, the Ti–N bond in the N1*s* spectra (Figure S5c) was in line with the Ti-N component positioned at 455.5 eV in the Ti 2*p* spectra.[67]

Besides, it is worth noting that there was a little peak at 457.3 eV, corresponding to the Ti-S band, which does not appear in the pristine Ti_3C_2 and N-MQDs.

These results indicate that the sulfur atom has functionalized the surface in the form of sulfonate and oxysulfide, and formed thiophene-S in the carbon skeleton of the Ti_3C_2 nanosheets. Besides, the co-doping with nitrogen can readily enhance the formation of thiophene-S, which stems from the fact that nitrogen doping can cause more defects of carbon framework. In other words, the sulfur bonds are primarily produced on the surface of Ti_3C_2 when sulfur is individually doped, which concurs with the highest thickness of S-MQDs in the AFM results (Figures 5g-h). From the Fourier transform infrared (FTIR) analysis, the obtained MQDs exhibited identical stretching vibrations, including Ti-O and C-O bands positioned at 612 and 1091 cm^{-1}, respectively (Figure 4g).[68] Besides, the peaks at 1417 and 1359 cm^{-1} were ascribed to the vibration of the C-N and C-S bonds, respectively, demonstrating the successful synthesis of three different MQDs doped by different heterogeneous elements. The Raman spectra of as-prepared MQDs (Figure 4h) are consistent with the spectrum of Ti_3C_2 in the previous study.[69] With regard to SN-MQDs, two broad peaks around 1328 and 1383 cm^{-1} could be attributed to the C-S and C-N vibrations, respectively, which were concordant with the FTIR results. The optical features of the 2D-QDs were further explored by ultraviolet-visible diffuse reflectance spectra (UV-vis DRS) (Figure 4i). The UV-vis DRS of the MQDs at 300 nm was corresponded to the n–π* electronic transition from the oxygen-containing functional groups (C=O). Meanwhile, the doped MQDs led to a 26 nm blue-shift compared with the original Ti_3C_2 due to the strong electronic affinity from the dopants. The optical band gap of MQDs was determined to be 2.4, 2.5 and 2.7 eV, corresponding to the SN-MQDs, N-MQDs and S-MQDs, respectively.

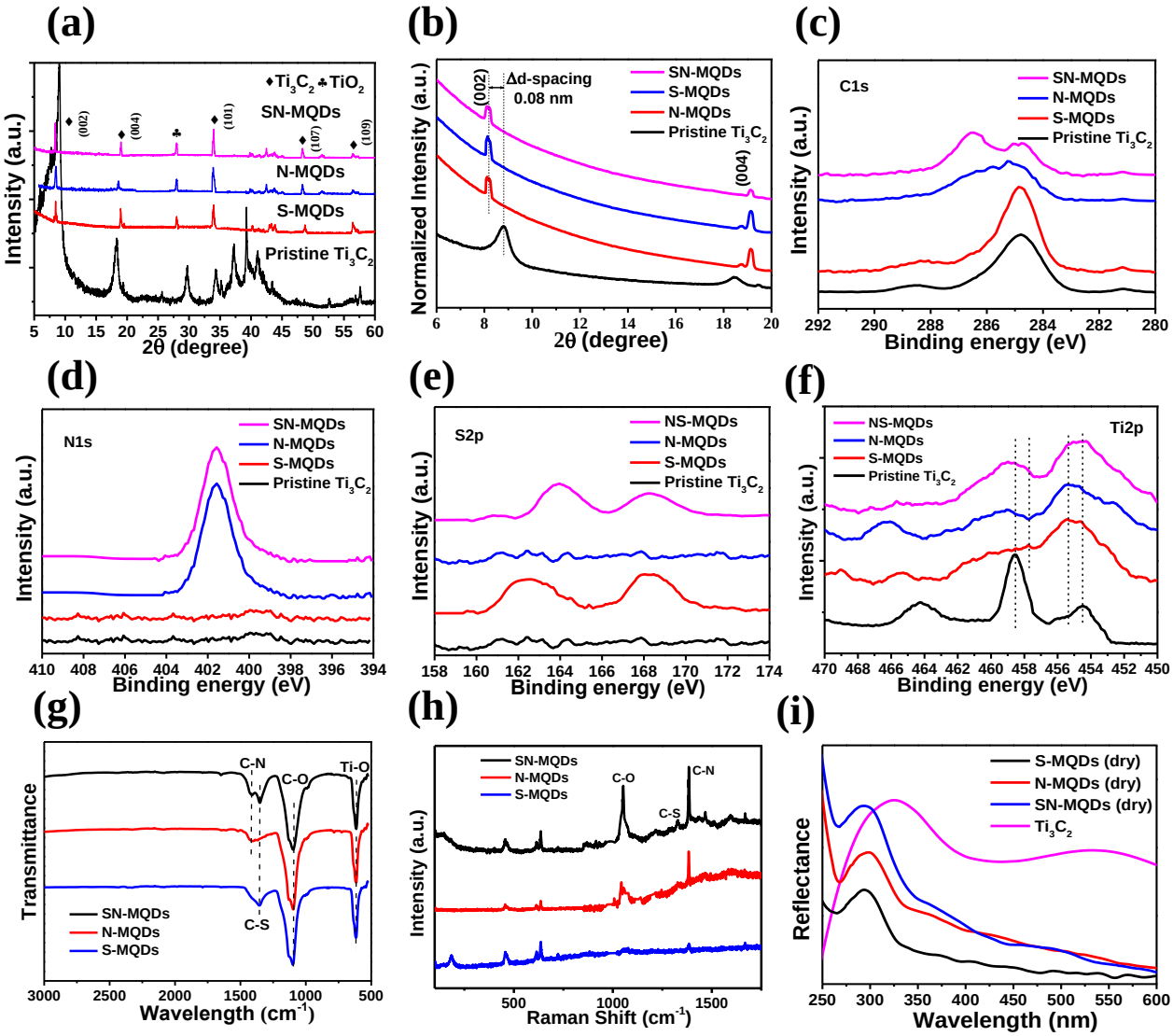

Figure 4. (a) XRD spectra of MQDs and pristine Ti_3C_2. (b) Normalized GIXRD patterns of pristine Ti_3C_2 and MQDs. High-resolution (c) C1*s*, (d) N1*s*, (e) S2*p* and (f) Ti2*p* XPS spectra of the MQDs and pristine Ti_3C_2. (g) FTIR and (h) Raman spectra of MQDs. (i) UV-vis DRS of pristine Ti_3C_2 and MQDs.

To investigate the microscopic morphology of the synthesized MQDs, a representative TEM image of the freshly obtained MQDs was acquired. As shown in Figure 5a-b, SN-MQDs formed a large piece with a bulky lateral size of ~50 nm, and N-MQDs showed a few pieces of assorted large blocks with a non-uniform size in the range of 15 and 35 nm. As for S-MQDs, the TEM image and the diameter size distribution are shown in Figure 5c, illustrating the formation of uniform ultra-small quantum dots with widths between 9 and 13 nm. Interestingly, there were two distinct lattice fringes closely arranged together as presented in the HRTEM image of SN-MQDs

(Figure 5d). One lattice spacing is 0.752 nm, while the other is 0.262 nm corresponding to the (101) lattice of an individual Ti_3C_2 layer. We speculated that there may be two kinds of doping products present in SN-MQDs. As for N-MQDs, they exhibited parallel arrangement (Figure 5e), while S-MQDs separately arranged (Figure 5f). Both have a lattice spacing of 0.262 nm, which denotes the (101) crystal plane. The different arrangement of MQDs caused the diverse lateral size.

Based on the atomic force microscopy (AFM) analysis (Figure 5g-i), the thickness of prepared SN-MQDs infers that there are two different heights of nanosheets arranged together, corresponding to ca. 20.41 and 14.15 nm, respectively. This is in consonance with the two distinct lattice fringes in the TEM image (Figure 5d). Furthermore, the heights of N-MQDs and S-MQDs are dissimilar, giving rise to 8.67 and 25.2 nm, respectively.

The lateral size and thickness of doped MQDs are depicted in Figures S6 and S7. Interestingly, the thickness and lateral size of S-MQDs are larger and wider than those of N-MQDs. The main ingredients of the two MQDs are sulfur doped Ti_3C_2 (S-MQDs) and nitrogen doped Ti_3C_2 (N-MQDs), respectively. As for SN-MQDs, the two distinct lattice fringes exhibit different lateral size. One is the same as N-MQDs, while the other is between N-MQDs and S-MQDs. Besides, the two heights in SN-MQDs are between S-MQDs and N-MQDs. Based on the aforementioned results, it can be observed that SN-MQDs contain two doped Ti_3C_2, corresponding to sulfur and nitrogen co-doped Ti_3C_2 (SN-MQDs) with nitrogen doped Ti_3C_2 (N-MQDs). To obtain the size and height distributions, 200 particles were calculated and measured directly from the TEM and AFM images.

In order to study the role of TiO_2 particles in MQDs, we use TiO_2 nano powder and non-doped Ti_3C_2 after acid treatment as a comparison (Figure 6a). Neither the TiO_2 nor the non-doped Ti_3C_2 exhibited fluorescence property after performing identical hydrothermal process. Besides, the SEM image of the formed TiO_2 in SN-MQDs is shown in Figure S8a, and the corresponding sulfur and nitrogen doped Ti_3C_2 is illustrated in Figure S8b. From the results of SEM, the sizes of Ti_2C_3 and TiO_2 are in great difference and there are separated. The SEM-EDS (energy dispersive spectrometer) elemental mapping images are shown in Figure S8c. Despite the generation of TiO_2 in MQDs, it does not produce fluorescence, hence does not affect the fluorescence properties of MQDs.

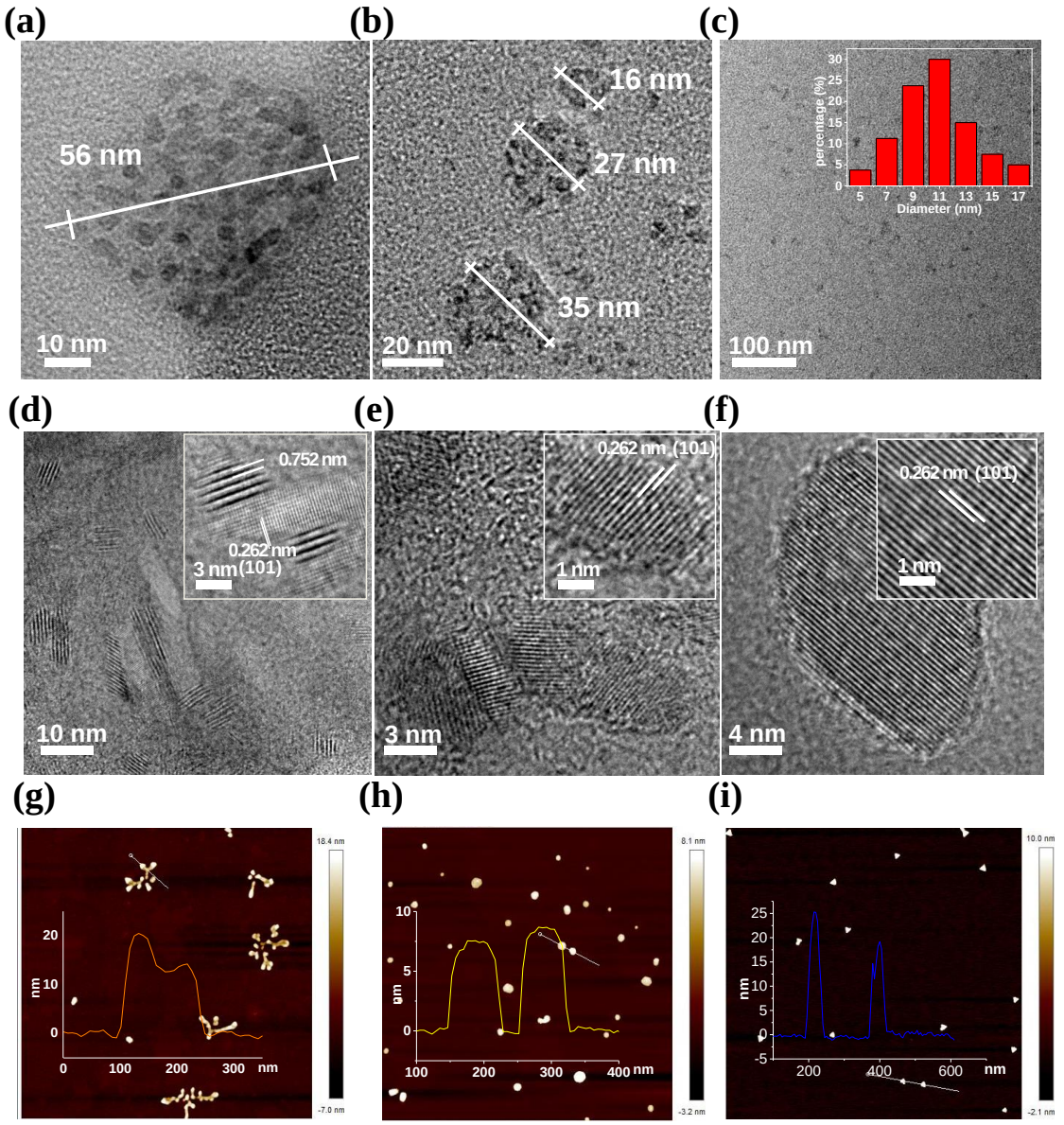

Figure 5. TEM images of (a) SN-MQDs, (b) N-MQDs and (c) S-MQDs. Diameter size distribution of S-MQDs was shown in the inset of (c) at top-right. HRTEM images of (d) SN-MQDs, (e) N-MQDs and (f) S-MQDs. Inset (top-right): Enlarged view of the HRTEM images. AFM images of (g) SN-MQDs, (h) N-MQDs and (i) S-MQDs. Inset (bottom-left): Thickness of the SN-MQDs, N-MQDs and S-MQDs.

To study the thermal stability of the synthesized MQDs, the HRTEM images of Ti_3C_2 before and after acid treatment are shown in Figure S9. It can be easily seen from the images that the large piece of Ti_3C_2 was divided into small pieces. PL spectra of synthesized S-MQDs under different hydrothermal time are shown in Figure 6b. Six hours after the hydrothermal process, Ti_3C_2 began to exhibit fluorescence property. However, when the time reaches 24 h, Ti_3C_2 no longer endows fluorescence properties, indicating the completely oxidized of Ti_3C_2

nanosheet. The TEM and the corresponding selected area electron diffraction (SAED) images are shown in Figure 6c-d. It can be seen from the SAED image that many grains are formed in the S-MQDs because of the generation of MXene QDs. Despite the irregular surface shape of the S-MQDs, the internal structure is well preserved.

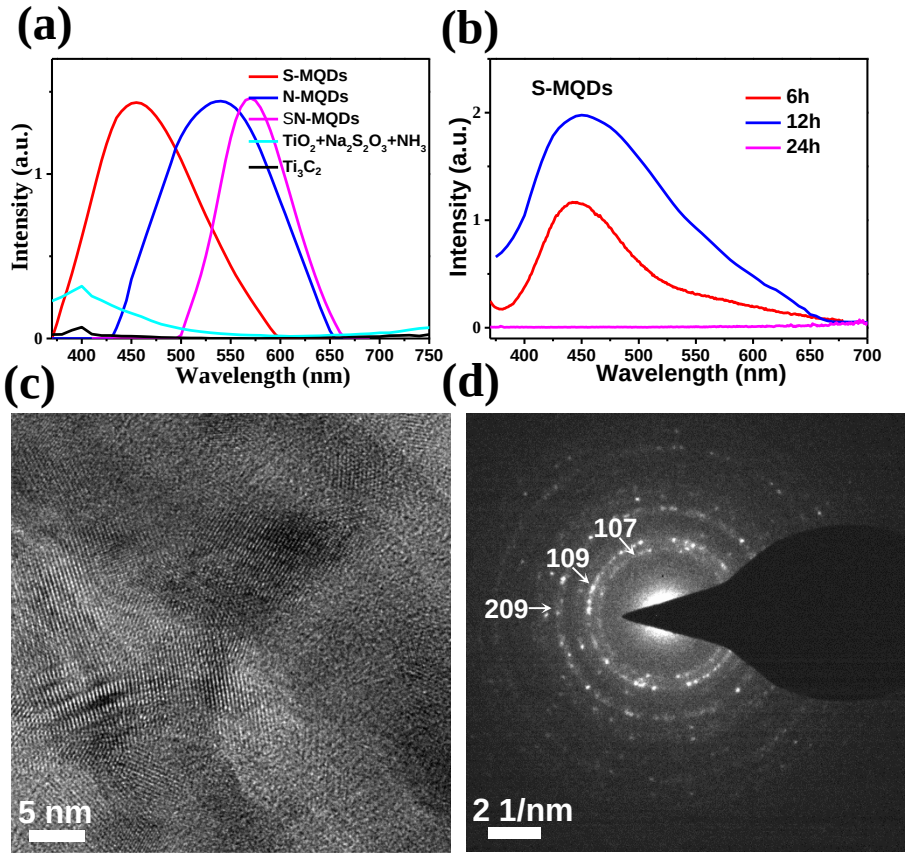

Figure 6. (a) PL spectra (UV light of 360 nm) of S-MQDs, N-MQDs, N-MQDs, and TiO_2 (doped with Na_2SO_4 and NH_3) and Ti_3C_2 after acid treatment (identical hydrothermal process without doping). (b) PL spectra of synthesized S-MQDs under different hydrothermal time. (c) TEM image and (d) SAED pattern of S-MQDs.

Herein, the bond order-bond length (BO-BL) distribution of pristine Ti_3C_2 QDs, and doped Ti_3C_2 QDs was analyzed (Figure 7). The calculation of bond order is based on the Mulliken population method.[70] The bond order indicates the bond strength since the larger the bond order is, the stronger the chemical bond is, which mainly shows an inverse correlation with the bond length. For the four different types of Ti_3C_2 QDs, the BO-BL distribution of Ti-O is localized with high BO and short BL, while the Ti-C presents a more extended BO-BL distribution with broad BO and long BL. This is because the Ti-C is a strong covalent bond, whereas the Ti-O is a relatively weak electrovalent bond. The bond characteristics of N and S doping at Ti_3C_2 QDs are different. The BO-

BL distribution of Ti-S is localized with short bond length for all types of Ti_3C_2-QDs, while the BO-BL distribution of Ti-N in SN-MQDs is more expansion with two types of Ti-N bonding. One is a strong Ti-N bond with short bond length, while the other is a weak bond with long bond length (similar to the hydrogen bonding in SN-MQDs). As such, based on the bonding character, water molecules on the SN-MQDs and N-MQDs surfaces can construct stalwart bridge-like hydrogen-bonded networks between the Ti_3C_2 particles.

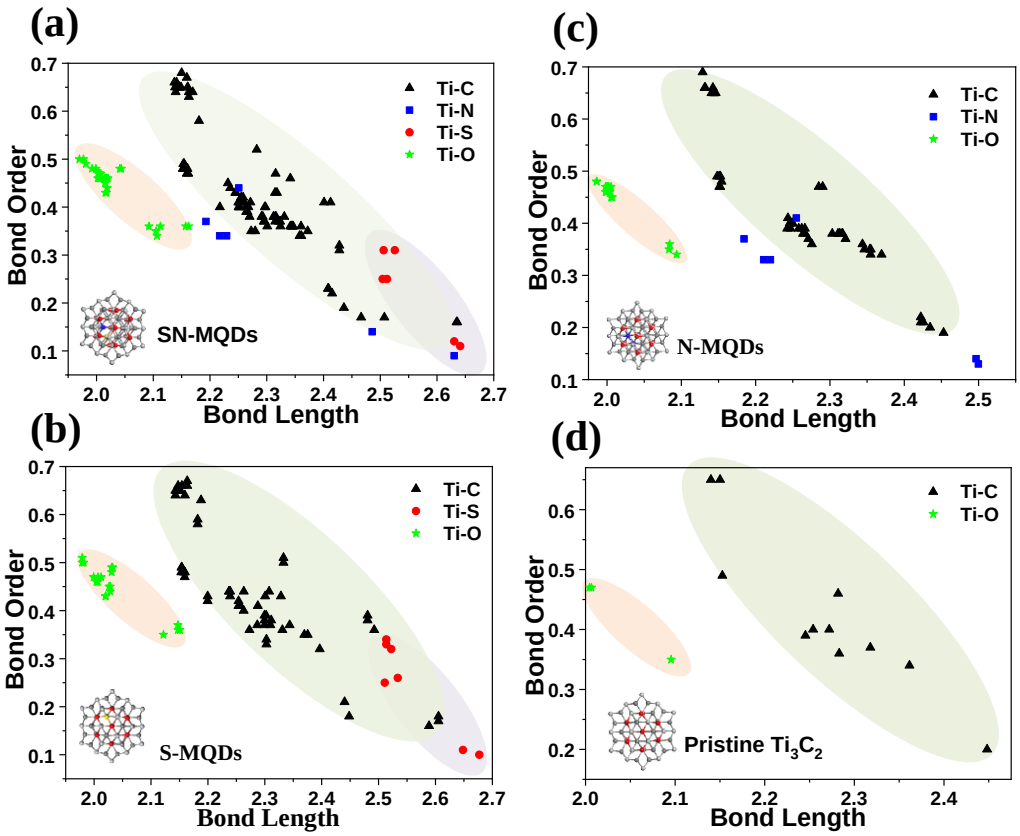

Figure 7. Bond order-bond length (BO-BL) distribution of four types Ti_3C_2 QDs: (a) SN-MQDs, (b) S-MQDs, (c) N-MQDs, and (d) pristine Ti_3C_2 QDs.

Due to the fact that white light emission is the most broadly utilized application in LED industry, special interest has been drawn to the white light-emitting diodes (WLEDs), but the technological challenges of investigating reliable and stable WLEDs are still up in the air at present.[71,72] As a virtually monochromatic light resource, the LEDs cannot be directly exploited for the generation of white light, which requires a broadband region of the visible spectra. Thus far, luminescent composites based on carbon dots (CD) have received increasing attentions in LEDs, and especially WLEDs.[73,74] However, the emission quench in the solid state makes it difficult to directly apply to LEDs. It is essential to develop high performance and strongly emitting full-color QDs-based

phosphors, with well dispersed in matrices and environmentally protected. Herein, the prepared white-color MQDs (W-MQDs) through SN-MQDs, N-MQDs and S-MQDs are mixed homogeneously with polyvinylpyrrolidone (PVP) due to excellent water solubility of MQDs. PVP is a commonly employed component with cost-effective and low toxicity, which exhibits a great solubility and colourless in aqueous solution. Thus, WLEDs were constructed and successfully operated under 365 nm irradiation and a voltage of 3.0 V. The PL photographs of the W-MQDs/PVP composites are indicated in Figure 8a. Because of the superior solubility of the aqueous solution of MQDs and PVP, a uniform and stable white light is obtained. Figure 8b shows the PL spectra of visible-light-emitting MQDs under 360 nm emission, and their maximum emission peaks of single color were 445, 540 and 580 nm for S-MQDs, N-MQDs and SN-MQDs, respectively. The emission wavelength of the prepared W-MQDs were expressed by the chromaticity indexes such as CIE 1931 (Figure 8c). The CIE coordinates of (0.31, 0.35) were located near the centre of the picture. The emission spectra of W-MQDs manifested high time stability under 360 nm emission (Figures 8d-e and S10). There is only a slight decrease in the PL intensity, but the typical shape of PL spectra is barely changed even after 30 days (Figure 8e). Due to the good water solubility, wide range emission spectrum and long-term stability, MQDs exhibits a virtuous application prospects in the field of WLED.

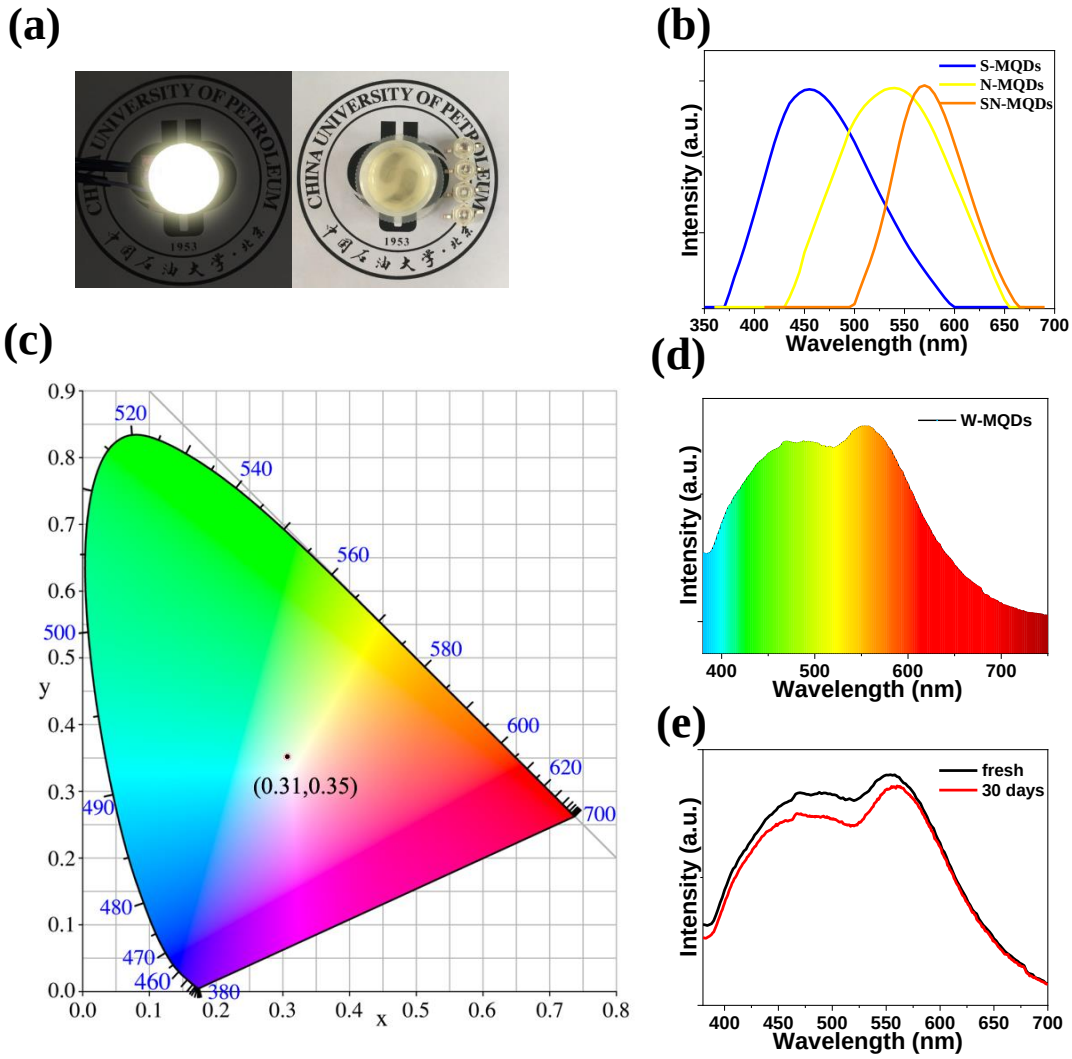

Figure 8. (a) Fluorescence images of the W-MQDs/PVP composite under 365 emissive chips. (b) PL spectra of visible-light-emitting MQDs under 360 nm emission. (c) Chromaticity diagram (CIE 1931) coordinates of W-MQDs/PVC under 360 nm emission, (0.31, 0.35). (d) Emission spectrum of W-MQDs under 360 nm emission. (e) Fluorescence spectra of the fresh W-MQDs and after 30 days under 360 nm emission.

CONCLUSION

In summary, by employing layered Ti_3C_2 MXene nanosheets as the starting material, novel photoluminescent SN-MQDs, N-MQDs and S-MQDs were successfully developed with the use of ammonia water and sodium thiosulfate as the nitrogen and sulfur precursors, respectively. The obtained MQDs exhibited a multi-color of blue, yellow and orange luminescence (under the excitation of 360 nm), which have not been reported in the literature studies of MQDs up to now. Fascinatingly, the synthesized MQDs had an excitation-independent and similar PL

emission in the solid state, while the emission was red-shifted with a fluorescence enhancement in the aqueous solution. The PL mechanism indicated that the construction of stalwart bridge-like hydrogen-bonded networks between the MQDs by highly ordered bound water on the doped MQDs surface can lead to the immobilization of the C=O and C-O bonds of the MQDs and vastly strengthen the rigidity of the entire system, resulting in increased lateral size and fluorescence enhancement (lifetime and QY). The decline of the band gap owing to the π-electron delocalization is responsible for the red-shift of the emissive spectra. Particularly, full-color MQDs were found to be very suitable for WLEDs with robust stability and efficiency. As such, the novel multi-color MQDs reported herein will broaden the technological applications, including sensing, bioimaging, electronics and solar cells.

Experimental Section

Synthesis of Ti_3C_2 MXene

Ti_3C_2Tx was synthesized using an etching route from our previously reported method.[67] Ti_2AlC (>92 wt%, Aladdin reagent Co., China) and TiC (99%, Aladdin reagent Co., China) were used to synthesize Ti_3AlC_2 powder in a 1:1 molar ratio by ball-milling for 16 h. The product was crushed using a mortar and pestle after heating at 1350 °C for 2 h in the Ar atmosphere with a heating rate 5 °C/min. 10 g of the obtained powder was added into a HF solution (50 mol%, ≈100 mL, Aladdin reagent Co., China) at 25 °C for 2 h. The resulting suspension was then washed several times using deionized water and centrifuged to separate the powders. Lastly, the wet sediments (Ti_3C_2) were dried in a vacuum oven at 70 °C for 14 h.

Synthesis of Doped MXene Quantum Dots

A mixture of HNO_3 and H_2SO_4 (1:3) was used to disperse Ti_3C_2 powder by heating at 100 °C for 12 h. The solution was diluted with 100 mL of deionized water and cooled to 25 °C in an ice-bath. The obtained products were added with NaOH until the pH reached ~7. To obtain SN-MQDs (S and N co-doped), 0.05 g of $Na_2S_2O_3$ and 200 µL of $NH_3 \cdot H_2O$ were added to 20 mL of treated Ti_3C_2 in the 50 mL Teflon-lined, stainless-steel autoclave, and the mixture was heated at 150 °C for 12 h. After that, a 1,000 Da dialysis membrane was used to first dialyze the reaction mixture for 2 days for isolation and purification. Subsequently, further purification was carried out by using a dialysis bag against ultrapure water. The ultrapure water was renewed every 16 h until no Na^+ was detected in the ultrapure water. Meanwhile, the nitrogen-doped MXene quantum dots (N-MQDs) and sulfur-doped MXene

quantum dots (S-MQDs) were prepared for comparisons by using ammonia water and sodium thiosulfate as the doping precursors, respectively, while the other processes are identical to the SN-MQDs.

DFT calculation approaches

The structural relaxation of all the models are performed by the Vienna *Ab initio* Simulation Package (VASP).[75,76] The bond order vs. bond length (BO-BL) distribution is calculated by the Cambridge Sequential Total Energy Package (CASTEP).[77] The Perdew-Burke-Ernzerhof (PBE) within generalized gradient approximation (GGA)[78] with the exchange-correlation potential was used. The kinetic energy cutoff of 580 eV is taken for the projector augmented plane wave (PAW) method.[79] The 2 × 2 × 3 *K*-point mesh is adopted. The convergence criteria for the energy and force are 10^{-5} eV and 0.01 eV/Å per atom, respectively.

Optical band gap calculation

The Kubelka-Munk equation is used to calculate the absorption of the dry samples:

$$F(R_\infty) = K/S = (1-R_\infty)^2 / 2R_\infty \quad (1)$$

where *K* is scattering coefficient, S is absorption coefficient and $R_\infty = R_{sample} = R_{standard}$.

In the case of a direct band gap semiconductor, the related equation of the band gap *Eg* and absorption coefficient α is shown below:[80]

$$\alpha h\nu = C_1(h\nu - Eg)^{1/2} \quad (2)$$

where α is absorption coefficient, *hν* is the photon energy and C_1 is a proportionality constant.

Fabrication of WLEDs from MQDs

Commercially available 365 nm emissive chips (SMD LED 2835) were purchased and used at the bottom of the LED base. First of all, we added 0.1 g of the dried powder to 1 mL of water to obtain a solution of MQDs. Then, the SN-MQDs, N-MQDs and S-MQDs (aqueous solution) were mixed with volume ratios of 1:1.2:1.2 to fabricate the white-color MQDs (W-MQDs). Then 2 mL of mixed W-MQDs and 0.5 g of polyvinylpyrrolidone (PVP) were homogeneously mixed to obtain the W-MQDs/PVP composite

material. After maintaining and aging for 3 days at room temperature, the W-MQDs/PVP composite material was covered on the 365 nm emissive chips under a voltage of 3 V, and the WLEDs were obtained.

Characterizations

X-ray diffraction analysis (XRD, Bruker D8 Advance, Germany) was employed to investigate the phase purity and crystalline structure of the samples with Cu-Kα radiation operated at 40 Kv and 100 Ma. The GIXRD measurements were performed at the BL14B1 beamline of the Shanghai Synchrotron Radiation Facility (SSRF) using X-ray with a wavelength of λ = 1.38 Å.[81] A X-ray photoelectron spectroscopy (XPS, ThermoFisher Escalab 250Xi) was utilized to study the surface elemental composition with an Al Kα radiation source scattering of 0-5,000 Ev. The surface morphology of the particles was characterized by a scanning electron microscopy (SEM, Hitachi SU8010) using an accelerating voltage of 15 kV. Transmission electron microscopy (TEM), high resolution TEM (HRTEM) and energy dispersive X-ray spectroscopy (EDS) were performed by Model JEM-2100 with a voltage at 200 kV. The functional groups of the samples were measured by utilizing a Fourier transform infrared spectroscopy (FTIR, Bruker 70V, USA). An ultraviolet-visible spectrometer (UV-Vis, Jasco V-570) was used to analyze the UV-vis diffuse reflectance spectra (UV-vis DRS). A Mastersizer 2000 (UK) was used for DLS and three measurements were acquired for 1 mL of each sample and averaged. The size estimates were obtained by intensity%. The fluorescence measurements (τ) were performed with a Cary Eclipse fluorescence spectrophotometer (FLS980, Techcomp Ltd., China). The measured PL decay curves were deconvoluted utilized a multi-exponential function:

$$I(t) = \sum_i A_i e^{\frac{-t}{\tau_i}} \tag{3}$$

The average lifetimes were obtained by the following equation:

$$\langle \tau \rangle = \sum_i A_i \tau_i^2 / \sum_i A_i \tau_i \tag{4}$$

where A_i and τ_i represent the amplitude and lifetime, respectively, of the individual components for multi-exponential decay profiles.

ASSOCIATED CONTENT

Supporting Information

SEM image and TEM-EDS elemental mapping images of the pristine Ti_3C_2 sheet, time-dependent PL spectra and UV-vis absorption spectra, PL spectra under different pH values, wide-scan XPS spectra and High-resolution XPS spectra, thickness distribution and lateral size of the prepared samples, PL spectra of MQDs in the dry state and redispersed in water and alcohol, time-dependent fluorescence spectra of W-MQDs, photoluminescence quantum yield and PL lifetimes (τ) of the as-synthesized MQDs

AUTHOR INFORMATION

Corresponding Author

*Quan Xu: xuquan@cup.edu.cn

*Neng Li: lineng@whut.edu.cn

*Wee-Jun Ong: weejun.ong@xmu.edu.my

ACKNOWLEDGMENT

Q. Xu thanks Beijing Nova Program Interdisciplinary Studies Cooperative project (No. Z181100006218138), Science Foundation of China University of Petroleum-Beijing (No. 2462018BJC004). N. Li thanks financially supported by the National Natural Science Foundation of China (No. 11604249), the Fok Ying-Tong Education Foundation for Young Teachers in the Higher Education Institutions of China (No. 161008), the Foundation of the State Key Laboratory of Optical Fiber and Cable Manufacture Technology (No. SKLD1602), the State Key Laboratory of Refractors and Metallurgy, the Fundamental Research Funds for the Central Universities, and the research board of the State Key Laboratory of Silicate Materials for Architectures. W.-J. Ong acknowledges financial assistance and faculty start-up supports (Xiamen University Malaysia Research Fund, XMUMRF/2019-C3/IENG/0013) from Xiamen University.

References

[1] Xu, Y., Wang, X., Zhang, W. L., Lv, F., Guo, S., Recent progress in two-dimensional inorganic quantum dots, Chem. Soc. Rev. 47 (2018) 586-625.
[2] Li, H., Tay, R. Y., Tsang, S. H., Zhen, X., Teo, E. H. T., Controllable synthesis of highly luminescent boron nitride quantum dots, Small 11 (2015) 6491-6499.
[3] Lei, Z., Xu, S., Wan, J., Wu, P., Facile preparation and multifunctional applications of boron nitride quantum dots, Nanoscale 7 (2015) 18902-18907.
[4] Kormányos, A., Zólyomi, V., Drummond, N. D., Burkard, G., Spin-orbit coupling, quantum dots, and qubits in monolayer transition metal dichalcogenides, Phys. Rev. X 4 (2014) 011034.
[5] Zhou, K., Zhang, Y., Xia, Z., Wei, W., As-prepared MoS2 quantum dot as a facile fluorescent probe for long-term tracing of live cells, Nanotechnology 27 (2016) 275101.
[6] Abdolmohammad-Zadeh, H., and Rahimpour, E., A novel chemosensor based on graphitic carbon nitride quantum dots and potassium ferricyanide chemiluminescence system for Hg (II) ion detection, Sens. Actuators, B 225 (2016) 258-266.
[7] Wang, W., Jimmy, C. Y., Shen, Z., Chan, D. K., Gu, T., gC 3 N 4 quantum dots: direct synthesis, upconversion properties and photocatalytic application, Chem. Commun. 50 (2014) 10148-10150.
[8] Ong, W.-J., Tan, L.-L., Ng, Y. H., Yong, S.-T., Chai, S.-P., Graphitic carbon nitride (g-C3N4)-based photocatalysts for artificial photosynthesis and environmental remediation: are we a step closer to achieving sustainability?, Chem. Rev. 116 (2016) 7159-7329.
[9] Zhang, H., Ultrathin two-dimensional nanomaterials, ACS nano 9 (2015) 9451-9469.
[10] Xu, M., Liang, T., Shi, M., Chen, H., Graphene-like two-dimensional materials, Chem. Rev. 113 (2013) 3766-3798.
[11] Sakamoto, R., Hoshiko, K., Liu, Q., Yagi, T., Nagayama, T., Kusaka, S., Tsuchiya, M., Kitagawa, Y., Wong, W.-Y., Nishihara, H., A photofunctional bottom-up bis (dipyrrinato) zinc (II) complex nanosheet, Nat. Commun. 6 (2015) 6713.
[12] Sakamoto, R., Yagi, T., Hoshiko, K., Kusaka, S., Matsuoka, R., Maeda, H., Liu, Z., Liu, Q., Wong, W. Y., Nishihara, H., Photofunctionality in Porphyrin‐Hybridized Bis (dipyrrinato) zinc (II) Complex Micro‐and Nanosheets, Angewandte Chemie 129 (2017) 3580-3584.
[13] Deng, D., Novoselov, K., Fu, Q., Zheng, N., Tian, Z., Bao, X., Catalysis with two-dimensional materials and their heterostructures, Nat. Nanotechnol. 11 (2016) 218.
[14] Rao, C., Ramakrishna Matte, H., Maitra, U., Graphene analogues of inorganic layered materials, Angew. Chem.Int. Edit. 52 (2013) 13162-13185.
[15] Huang, X., Tan, C., Yin, Z., Zhang, H., 25th Anniversary Article: Hybrid Nanostructures Based on Two‐Dimensional Nanomaterials, Adv. Mater. 26 (2014) 2185-2204.
[16] Miró, P., Audiffred, M., Heine, T., An atlas of two-dimensional materials, Chem. Soc. Rev. 43 (2014) 6537-6554.
[17] Rim, Y. S., Bae, S. H., Chen, H., De Marco, N., Yang, Y., Recent progress in materials and devices toward printable and flexible sensors, Adv. Mater. 28 (2016) 4415-4440.
[18] Wang, L., Xiong, Q., Xiao, F., Duan, H., 2D nanomaterials based electrochemical biosensors for cancer diagnosis, Biosens. Bioelectron. 89 (2017) 136-151.
[19] Buzaglo, M., Shtein, M., Regev, O., Graphene quantum dots produced by microfluidization, Chem. Mater. 28 (2015) 21-24.
[20] Liu, F., Jang, M. H., Ha, H. D., Kim, J. H., Cho, Y. H., Seo, T. S., Facile synthetic method for pristine graphene quantum dots and graphene oxide quantum dots: origin of blue and green luminescence, Adv. Mater. 25 (2013) 3657-3662.
[21] Yoo, J. M., Kang, J. H., Hong, B. H., Graphene-based nanomaterials for versatile imaging studies, Chem. Soc. Rev. 44 (2015) 4835-4852.
[22] Li, H., Shao, F.-Q., Huang, H., Feng, J.-J., Wang, A.-J., Eco-friendly and rapid microwave synthesis of green fluorescent graphitic carbon nitride quantum dots for vitro bioimaging, Sens. Actuators, B 226 (2016) 506-511.
[23] Dong, H., Tang, S., Hao, Y., Yu, H., Dai, W., Zhao, G., Cao, Y., Lu, H., Zhang, X., Ju, H., Fluorescent MoS2 quantum dots: ultrasonic preparation, up-conversion and down-conversion bioimaging, and photodynamic therapy, ACS Appl. Mater. Interfaces 8 (2016) 3107-3114.
[24] Gu, W., Yan, Y., Cao, X., Zhang, C., Ding, C., Xian, Y., A facile and one-step ethanol-thermal synthesis of MoS 2 quantum dots for two-photon fluorescence imaging, J. Mater. Chem. B 4 (2016) 27-31.
[25] Zhao, W., Li, Y., Yang, S., Chen, Y., Zheng, J., Liu, C., Qing, Z., Li, J., Yang, R., Target-activated modulation of dual-color and two-photon fluorescence of graphene quantum dots for in vivo imaging of hydrogen peroxide, Anal. Chem. 88 (2016) 4833-4840.
[26] Wang, X., Wang, Y., He, H., Chen, X., Sun, X., Sun, Y., Zhou, G., Xu, H., Huang, F., Steering graphene quantum dots in living cells: lighting up the nucleolus, J. Mater. Chem. B 4 (2016) 779-784.

[27] Yuwen, L., Zhou, J., Zhang, Y., Zhang, Q., Shan, J., Luo, Z., Weng, L., Teng, Z., Wang, L., Aqueous phase preparation of ultrasmall MoSe 2 nanodots for efficient photothermal therapy of cancer cells, Nanoscale 8 (2016) 2720-2726.
[28] Yong, Y., Cheng, X., Bao, T., Zu, M., Yan, L., Yin, W., Ge, C., Wang, D., Gu, Z., Zhao, Y., Tungsten sulfide quantum dots as multifunctional nanotheranostics for in vivo dual-modal image-guided photothermal/radiotherapy synergistic therapy, ACS nano 9 (2015) 12451-12463.
[29] Gu, W., Yan, Y., Zhang, C., Ding, C., Xian, Y., One-step synthesis of water-soluble MoS2 quantum dots via a hydrothermal method as a fluorescent probe for hyaluronidase detection, ACS Appl. Mater. Interfaces 8 (2016) 11272-11279.
[30] Zhang, T., Zhao, H., Fan, G., Li, Y., Li, L., Quan, X., Electrolytic exfoliation synthesis of boron doped graphene quantum dots: a new luminescent material for electrochemiluminescence detection of oncogene microRNA-20a, Electrochim. Acta 190 (2016) 1150-1158.
[31] Zhu, X., Liu, J., Peng, H., Jiang, J., Yu, R., A novel fluorescence assay for inorganic pyrophosphatase based on modulated aggregation of graphene quantum dots, Analyst 141 (2016) 251-255.
[32] Kufer, D., Nikitskiy, I., Lasanta, T., Navickaite, G., Koppens, F. H., Konstantatos, G., Hybrid 2D–0D MoS2–PbS quantum dot photodetectors, Adv. Mater. 27 (2015) 176-180.
[33] Zhang, Q., Jie, J., Diao, S., Shao, Z., Zhang, Q., Wang, L., Deng, W., Hu, W., Xia, H., Yuan, X., Solution-processed graphene quantum dot deep-UV photodetectors, ACS nano 9 (2015) 1561-1570.
[34] Wang, H., Yuan, X., Wang, H., Chen, X., Wu, Z., Jiang, L., Xiong, W., Zeng, G., Facile synthesis of Sb2S3/ultrathin g-C3N4 sheets heterostructures embedded with g-C3N4 quantum dots with enhanced NIR-light photocatalytic performance, Appl. Catal., B 193 (2016) 36-46.
[35] Gao, W., Wang, M., Ran, C., Li, L., Facile one-pot synthesis of MoS 2 quantum dots–graphene–TiO 2 composites for highly enhanced photocatalytic properties, Chem. Commun. 51 (2015) 1709-1712.
[36] Liu, J., Zheng, M., Shi, X., Zeng, H., Xia, H., Amorphous FeOOH quantum dots assembled mesoporous film anchored on graphene nanosheets with superior electrochemical performance for supercapacitors, Adv. Funct. Mater. 26 (2016) 919-930.
[37] Li, Z., Qin, P., Wang, L., Yang, C., Li, Y., Chen, Z., Pan, D., Wu, M., Amine-enriched graphene quantum dots for high-pseudocapacitance supercapacitors, Electrochim. Acta 208 (2016) 260-266.
[38] Anasori, B., Lukatskaya, M. R., Gogotsi, Y., 2D metal carbides and nitrides (MXenes) for energy storage, Nat. Rev. Mater. 2 (2017) 16098.
[39] Zhang, X., Zhang, Z., Zhou, Z., MXene-based materials for electrochemical energy storage, Journal of energy chemistry 27 (2018) 73-85.
[40] Wei, X., An, Q., Wei, Q., Yan, M., Wang, X., Li, Q., Zhang, P., Wang, B., Mai, L., A Bowknot-like RuO 2 quantum dots@ V 2 O 5 cathode with largely improved electrochemical performance, Phys. Chem. Chem. Phys. 16 (2014) 18680-18685.
[41] Chao, D., Zhu, C., Xia, X., Liu, J., Zhang, X., Wang, J., Liang, P., Lin, J., Zhang, H., Shen, Z. X., Graphene quantum dots coated VO2 arrays for highly durable electrodes for Li and Na ion batteries, Nano Lett. 15 (2014) 565-573.
[42] Naguib, M., Kurtoglu, M., Presser, V., Lu, J., Niu, J., Heon, M., Hultman, L., Gogotsi, Y., Barsoum, M. W., Two‐dimensional nanocrystals produced by exfoliation of Ti3AlC2, Adv. Mater. 23 (2011) 4248-4253.
[43] Lin, H., Wang, C., Wu, J., Xu, Z., Huang, Y., Zhang, C., Colloidal synthesis of MoS 2 quantum dots: size-dependent tunable photoluminescence and bioimaging, New J. Chem. 39 (2015) 8492-8497.
[44] Zhang, X., Wang, H., Wang, H., Zhang, Q., Xie, J., Tian, Y., Wang, J., Xie, Y., Single‐Layered Graphitic‐C3N4 Quantum Dots for Two‐Photon Fluorescence Imaging of Cellular Nucleus, Adv. Mater. 26 (2014) 4438-4443.
[45] Sang, X., Xie, Y., Lin, M.-W., Alhabeb, M., Van Aken, K. L., Gogotsi, Y., Kent, P. R., Xiao, K., Unocic, R. R., Atomic Defects in Monolayer Titanium Carbide (Ti3C2T x) MXene, ACS nano 10 (2016) 9193-9200.
[46] Xue, Q., Zhang, H., Zhu, M., Pei, Z., Li, H., Wang, Z., Huang, Y., Huang, Y., Deng, Q., Zhou, J., Photoluminescent Ti3C2 MXene Quantum Dots for Multicolor Cellular Imaging, Adv. Mater. 29 (2017)
[47] Xu, G., Niu, Y., Yang, X., Jin, Z., Wang, Y., Xu, Y., Niu, H., Preparation of Ti3C2Tx MXene‐Derived Quantum Dots with White/Blue‐Emitting Photoluminescence and Electrochemiluminescence, Adv. Opt. Mater. 6 (2018) 1800951.
[48] Wang, Z., Xuan, J., Zhao, Z., Li, Q., Geng, F., Versatile cutting method for producing fluorescent ultrasmall MXene sheets, ACS nano 11 (2017) 11559-11565.
[49] Xu, Q., Ding, L., Wen, Y., Yang, W., Zhou, H., Chen, X., Street, J., Zhou, A., Ong, W.-J., Li, N., High Photoluminescence Quantum Yield of 18.7% by Nitrogen-Doped Ti3C2 MXene Quantum Dots, J. Mater. Chem. C (2018) 6360-6369.
[50] Sk, M. A., Ananthanarayanan, A., Huang, L., Lim, K. H., Chen, P., Revealing the tunable photoluminescence properties of graphene quantum dots, J. Mater. Chem. C 2 (2014) 6954-6960.
[51] Bailey, R. E., and Nie, S., Alloyed semiconductor quantum dots: tuning the optical properties without changing the particle size, J. Am. Chem. Soc. 125 (2003) 7100-7106.
[52] Li, F., Men, Z., Li, S., Wang, S., Li, Z., Sun, C., Study of hydrogen bonding in ethanol-water binary solutions by Raman spectroscopy, Spectrochim. Acta, Part A 189 (2018) 621-624.
[53] Li, Q., Zhou, M., Yang, M., Yang, Q., Zhang, Z., Shi, J., Induction of long-lived room temperature phosphorescence of carbon dots by water in hydrogen-bonded matrices, Nat. Commun. 9 (2018) 734.

[54] Zakharov, B. A., Kolesov, B. A., Boldyreva, E. V., Monitoring selected hydrogen bonds in crystal hydrates of amino acid salts: combining variable-temperature single-crystal X-ray diffraction and polarized Raman spectroscopy, Phys. Chem. Chem. Phys. 13 (2011) 13106-13116.
[55] Garczarek, F., and Gerwert, K., Functional waters in intraprotein proton transfer monitored by FTIR difference spectroscopy, Nature 439 (2006) 109-112.
[56] Wang, Y., Von Euw, S., Fernandes, F. M., Cassaignon, S., Selmane, M., Laurent, G., Pehau-Arnaudet, G., Coelho, C., Bonhomme-Coury, L., Giraud-Guille, M.-M., Water-mediated structuring of bone apatite, Nat. Mater. 12 (2013) 1144-1153.
[57] Ball, P., Water is an active matrix of life for cell and molecular biology, Proc. Natl. Acad. Sci. U. S. A. 114 (2017) 13327-13335.
[58] Chen, X., Sun, X., Xu, W., Pan, G., Zhou, D., Zhu, J., Wang, H., Bai, X., Dong, B., Song, H., Ratiometric photoluminescence sensing based on Ti 3 C 2 MXene quantum dots as an intracellular pH sensor, Nanoscale 10 (2018) 1111-1118.
[59] Zhu, J., Tang, Y., Yang, C., Wang, F., Cao, M., Composites of TiO2 nanoparticles deposited on Ti3C2 MXene nanosheets with enhanced electrochemical performance, J. Electrochem. Soc. 163 (2016) A785-A791.
[60] Tang, Y., Zhu, J., Yang, C., Wang, F., Enhanced supercapacitive performance of manganese oxides doped two-dimensional titanium carbide nanocomposite in alkaline electrolyte, J. Alloys Compd. 685 (2016) 194-201.
[61] Liu, X., and Dai, L., Carbon-based metal-free catalysts, Nat. Rev. Mater. 1 (2016) 16064.
[62] Gonbeau, D., Guimon, C., Pfister-Guillouzo, G., Levasseur, A., Meunier, G., Dormoy, R., XPS study of thin films of titanium oxysulfides, Surf. Sci. 254 (1991) 81-89.
[63] Yang, C., Que, W., Tang, Y., Tian, Y., Yin, X., Nitrogen and Sulfur Co-Doped 2D Titanium Carbides for Enhanced Electrochemical Performance, J. Electrochem. Soc. 164 (2017) A1939-A1945.
[64] Rakhi, R. B., Ahmed, B., Hedhili, M. N., Anjum, D. H., Alshareef, H. N., Effect of Postetch Annealing Gas Composition on the Structural and Electrochemical Properties of Ti2CTx MXene Electrodes for Supercapacitor Applications, Chem.Mater. 27 (2015) 5314-5323.
[65] Yang, H. G., Sun, C. H., Qiao, S. Z., Zou, J., Liu, G., Smith, S. C., Cheng, H. M., Lu, G. Q., Anatase TiO2 single crystals with a large percentage of reactive facets, Nature 453 (2008) 638.
[66] Dang, B. H. Q., Rahman, M., Macelroy, D., Dowling, D. P., Evaluation of microwave plasma oxidation treatments for the fabrication of photoactive un-doped and carbon-doped TiO 2 coatings, Anal. Chim. Acta. 206 (2012) 4113-4118.
[67] Wen, Y., Rufford, T. E., Chen, X., Li, N., Lyu, M., Dai, L., Wang, L., Nitrogen-doped Ti3C2Tx MXene electrodes for high-performance supercapacitors, Nano energy 38 (2017) 368-376.
[68] Boota, M., Anasori, B., Voigt, C., Zhao, M. Q., Barsoum, M. W., Gogotsi, Y., Pseudocapacitive Electrodes Produced by Oxidant‐Free Polymerization of Pyrrole between the Layers of 2D Titanium Carbide (MXene), Adv. Mater. 28 (2016) 1517-1522.
[69] Naguib, M., Mashtalir, O., Lukatskaya, M. R., Dyatkin, B., Zhang, C., Presser, V., Gogotsi, Y., Barsoum, M. W., One-step synthesis of nanocrystalline transition metal oxides on thin sheets of disordered graphitic carbon by oxidation of MXenes, Chem. Commun. 50 (2014) 7420-7423.
[70] Mulliken, R. S., Electronic population analysis on LCAO‐MO molecular wave functions. I, J. Chem. Phys. 23 (1955) 1833-1840.
[71] Gotta, J., Shalom, T. B., Aslanoglou, S., Cifuentes‐Rius, A., Voelcker, N. H., Elnathan, R., Shoseyov, O., Richter, S., Stable White Light‐Emitting Biocomposite Films, Adv. Funct. Mater. (2018) 1706967.
[72] Bando, K., Sakano, K., Noguchi, Y., Shimizu, Y., Development of high-bright and pure-white LED lamps, J. Light Visual Environ. 22 (1998) 1_2-1_5.
[73] Sun, M., Qu, S., Hao, Z., Ji, W., Jing, P., Zhang, H., Zhang, L., Zhao, J., Shen, D., Towards efficient solid-state photoluminescence based on carbon-nanodots and starch composites, Nanoscale 6 (2014) 13076-13081.
[74] Sun, C., Zhang, Y., Sun, K., Reckmeier, C., Zhang, T., Zhang, X., Zhao, J., Wu, C., William, W. Y., Rogach, A. L., Combination of carbon dot and polymer dot phosphors for white light-emitting diodes, Nanoscale 7 (2015) 12045-12050.
[75] Kresse, G., and Furthmüller, J., Efficiency of ab-initio total energy calculations for metals and semiconductors using a plane-wave basis set, Comput. Mater. Sci. 6 (1996) 15-50.
[76] Kresse, G., and Hafner, J., Ab initio molecular dynamics for liquid metals, Phys. Rev. B 47 (1993) 558-561.
[77] Clark, S. J., Segall, M. D., Pickard, C. J., Hasnip, P. J., Probert, M. I., Refson, K., Payne, M. C., First principles methods using CASTEP, Z. Kristallogr. - Cryst. Mater. 220 (2005) 567-570.
[78] Perdew, J. P., Burke, K., Ernzerhof, M., Generalized gradient approximation made simple, Phys. Rev. Lett. 77 (1996) 3865-3868.
[79] Blöchl, P. E., Projector augmented-wave method, Phys. Rev. B 50 (1994) 17953.
[80] Morales, A. E., Mora, E. S., Pal, U., Use of diffuse reflectance spectroscopy for optical characterization of un-supported nanostructures, Rev. Mex. Fis. 53 (2007) 18-22.
[81] Wang, Z.-K., Gong, X., Li, M., Hu, Y., Wang, J.-M., Ma, H., Liao, L.-S., Induced crystallization of perovskites by a perylene underlayer for high-performance solar cells, ACS Nano 10 (2016) 5479-5489.

The table of contents

Multiple-color emissive MXene quantum dots (MQDs) are prepared by employing hydrogen bonds as an adjustment method. White light-emitting diodes (WLEDs) with stable emission color by utilizing MQDs as an active layer have been achieved for the first time. The photoluminescence mechanism manifests that the construction of bridge-like hydrogen-bonded networks between MQDs by bound water gives rise to the immobilization of C=O and C-O bonds of MQDs and ameliorats the system's rigidity.

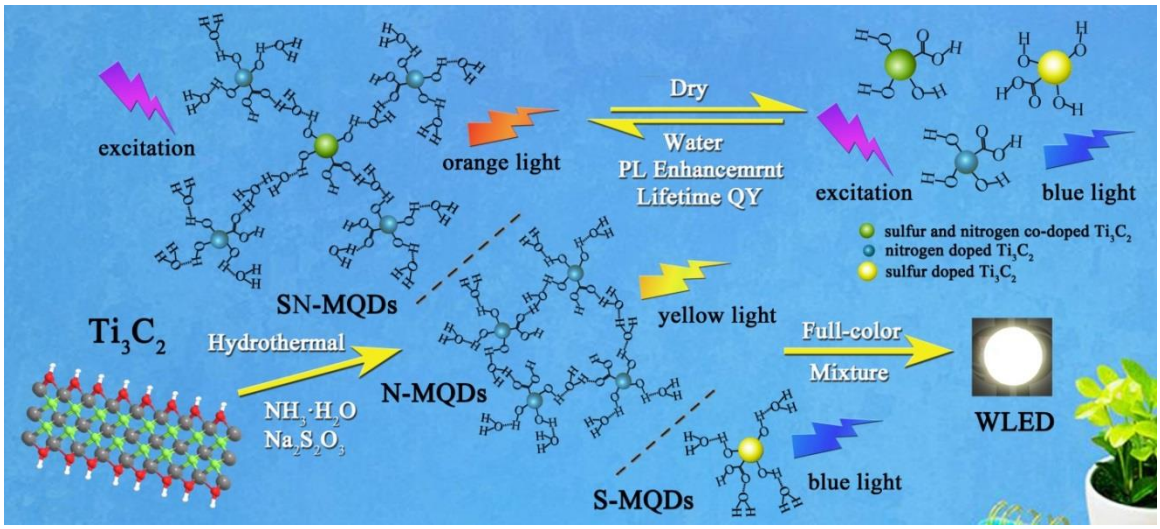

Supporting Information

Hydrochromic Full-Color MXene Quantum Dots through Hydrogen Bonding toward Ultrahigh-Efficiency White Light-Emitting Diodes

Quan Xu[=†*], Wenjing Yang[=†], Yangyang Wen[=†], Shengkun Liu[†], Zheng Liu[§], Wee-Jun Ong[ǁ#*], and Neng Li[‡*]

† State Key Laboratory of Heavy Oil Processing, Harvard SEAS-CUPB Joint Laboratory on Petroleum Science,China University of Petroleum-Beijing, 102249, China. E-mail: xuquan@cup.edu.cn

‡ State Key Laboratory of Silicate Materials for Architectures, Wuhan University of Technology, 430070, China. E-mail: lineng@whut.edu.cn

§ Centre for Programmable Materials, School of Materials Science and Engineering, Nanyang Technological University, 50 Nanyang Avenue, Singapore 637371, Singapore

ǁ School of Energy and Chemical Engineering, Xiamen University Malaysia, Selangor Darul Ehsan 43900, Malaysia. E-mail: weejun.ong@xmu.edu.my; ongweejun@gmail.com

College of Chemistry and Chemical Engineering, Xiamen University, Xiamen 361005, China

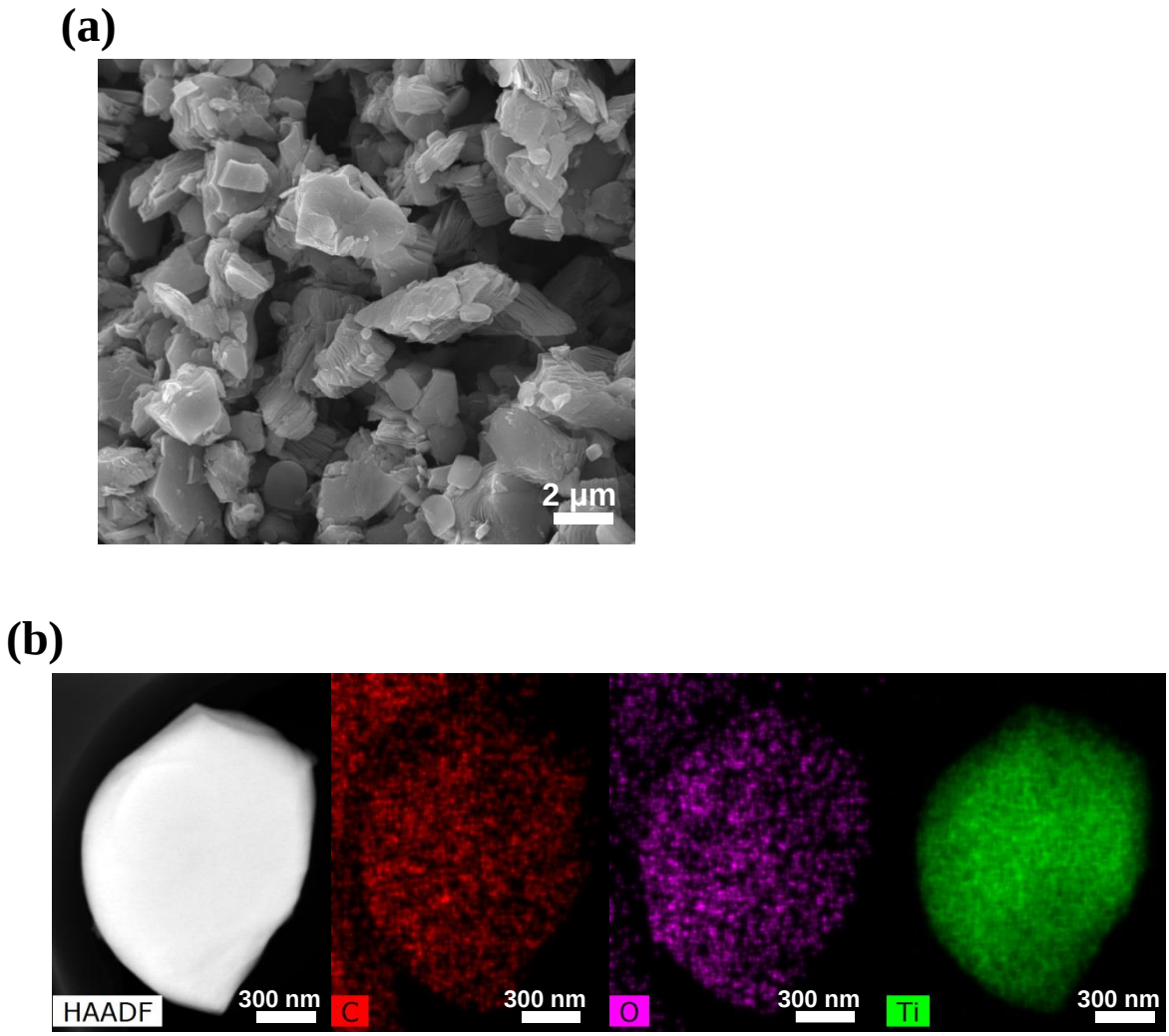

Figure S1. SEM image of (a) pristine Ti_3C_2 and (b) TEM-EDS elemental mapping images of the pristine Ti_3C_2 sheet.

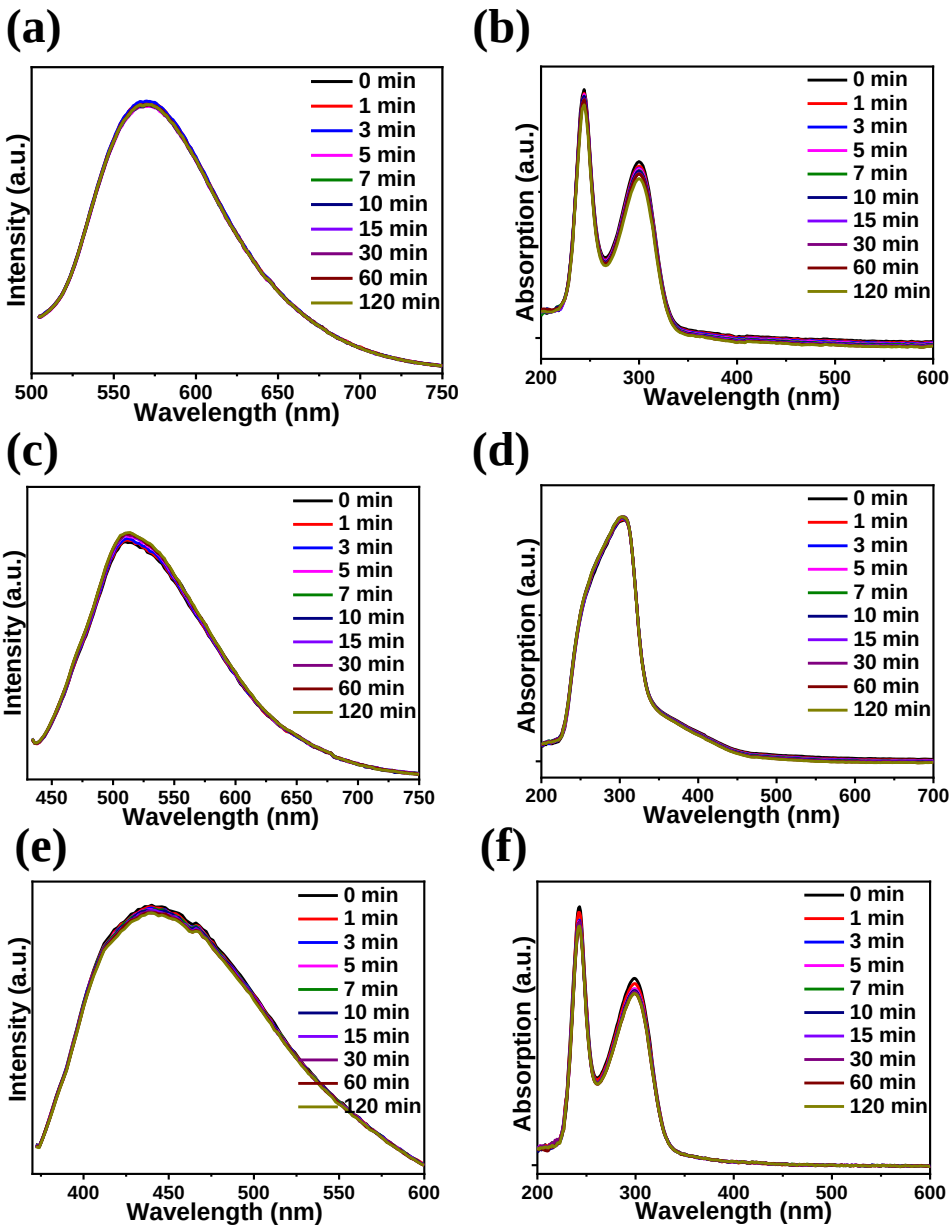

Figure S2. Time-dependent PL spectra and UV-vis absorption spectra of (a-b) SN-MQDs, (c-d) N-MQDs and (e-f) S-MQDs.

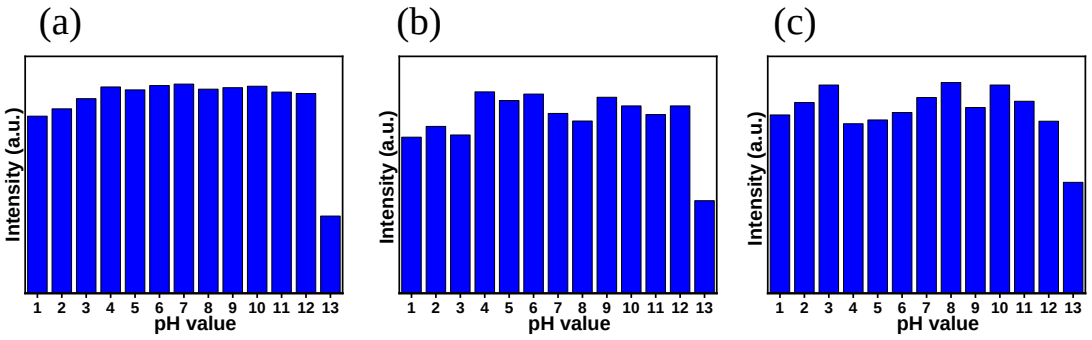

Figure S3. PL spectra of (a) SN-MQDs, (b) N-MQDs and (c) S-MQDs under different pH values.

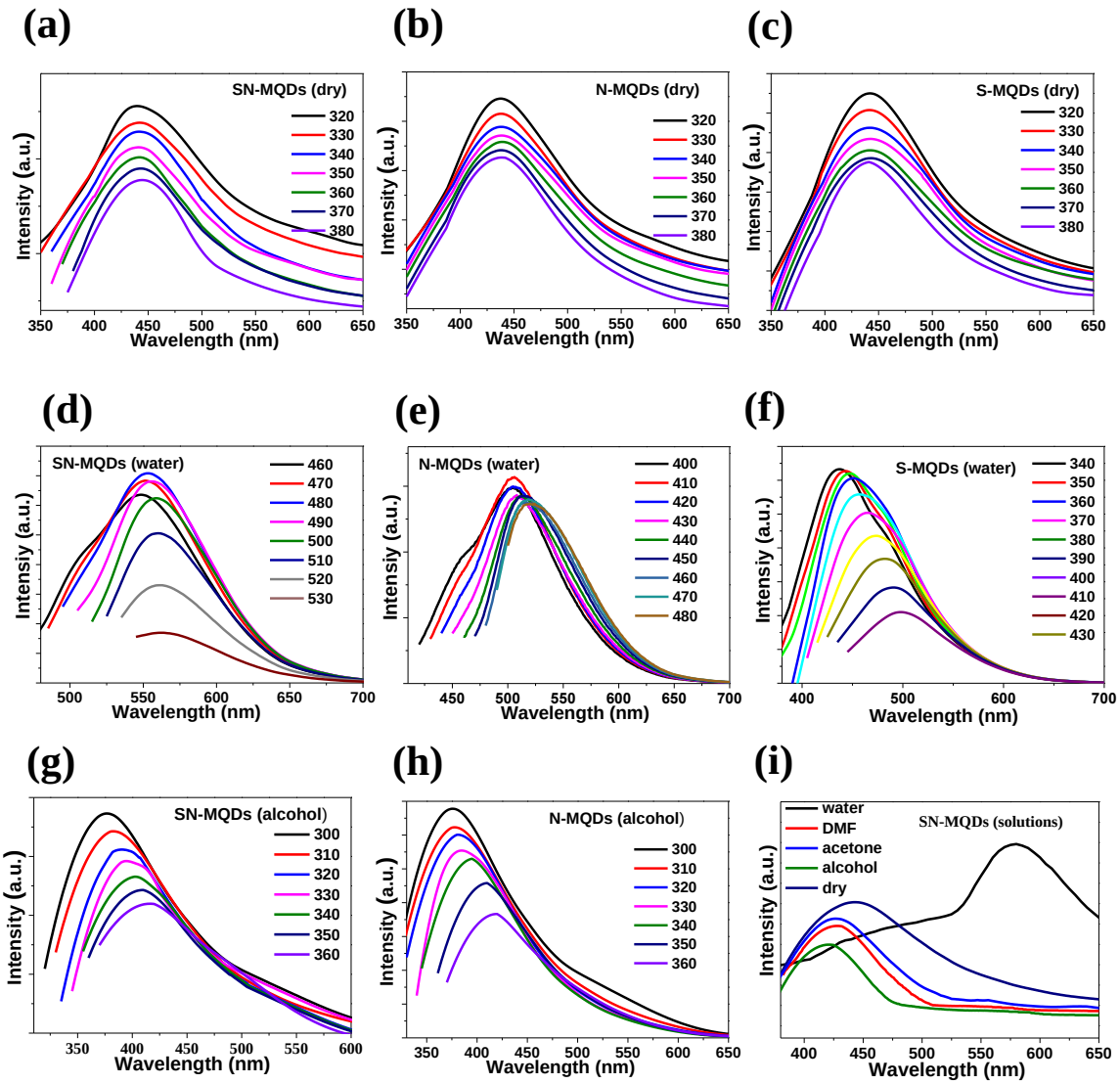

Figure S4. (a-c) PL spectra of MQDs in the dry state. PL spectra of MQDs redispersed in (d-f) water and (g-h) alcohol. (i) PL spectra of SN-MQDs in different solvents and water solution.

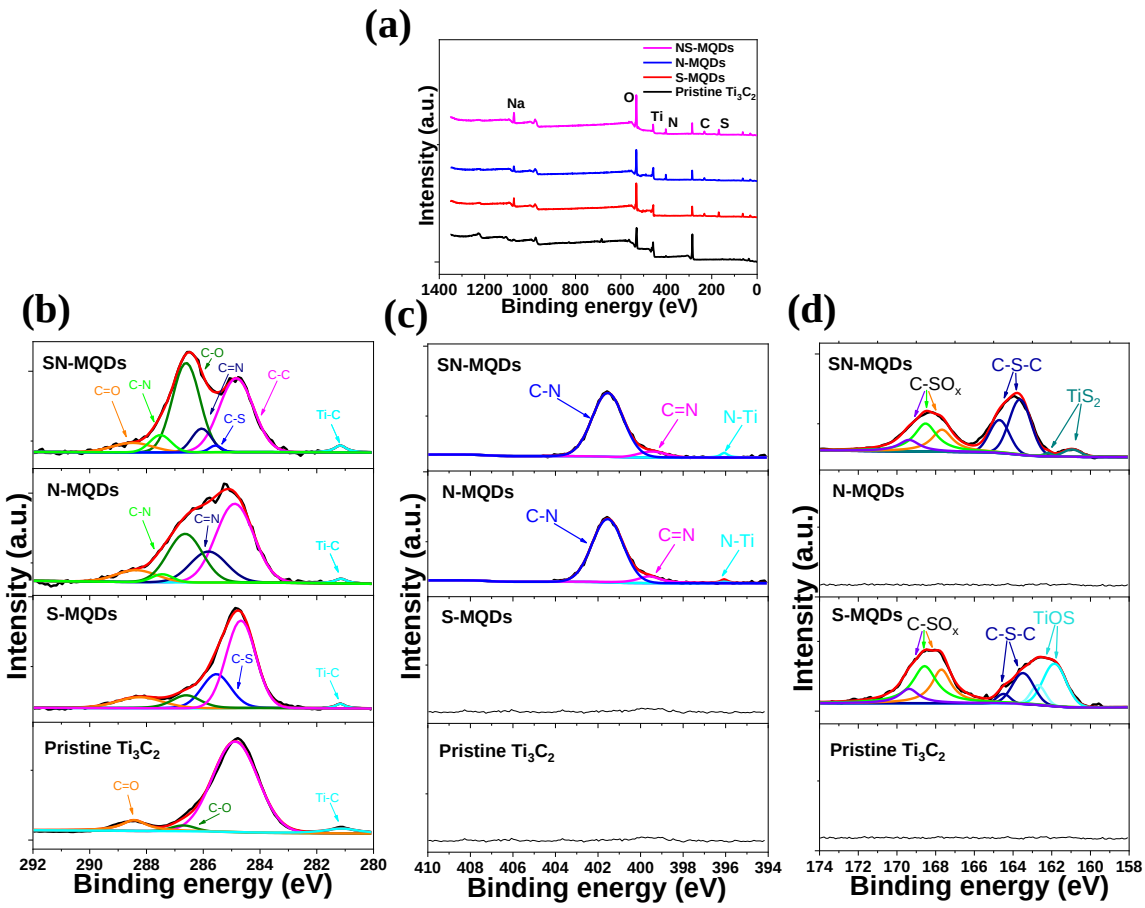

Figure S5. (a) Wide-scan XPS spectra for pristine Ti_3C_2 and MQDs. High-resolution XPS spectra of (b) C1*s*, (c) N1*s*, and (d) S2*p* XPS spectra for the pristine Ti_3C_2 and MQDs.

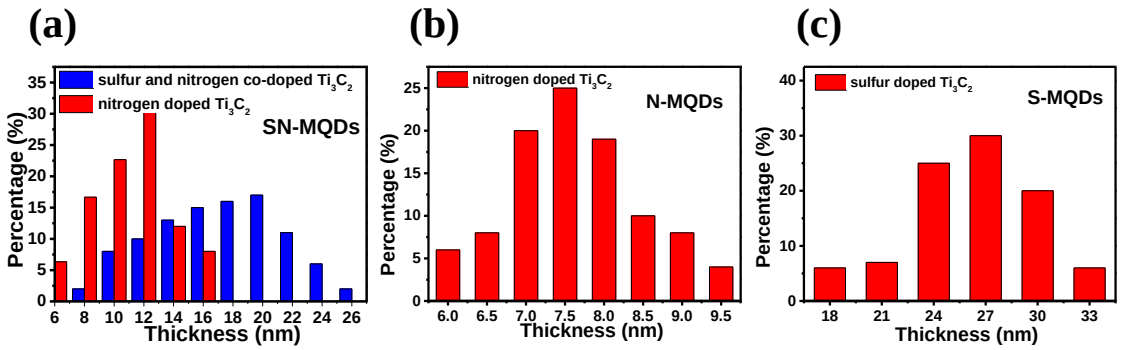

Figure S6. Thickness distribution of the prepared (a) SN-MQDs, (b) N-MQDs and (c) S-MQDs.

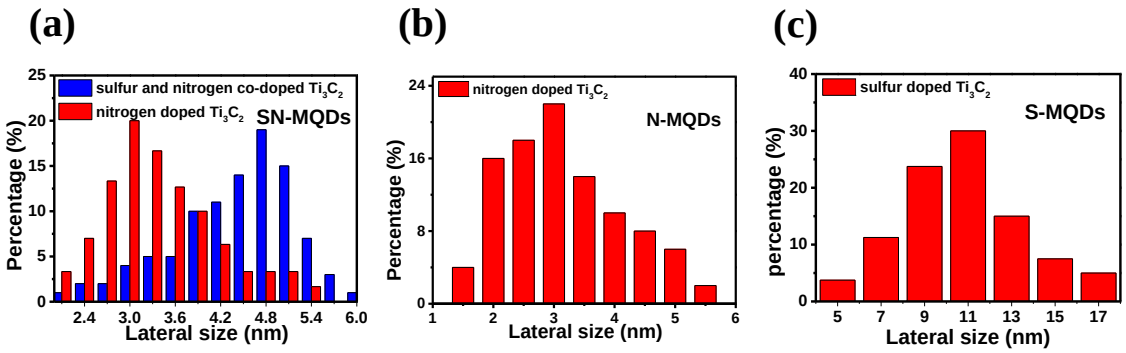

Figure S7. Lateral size of the prepared (a) SN-MQDs, (b) N-MQDs and (c) S-MQDs.

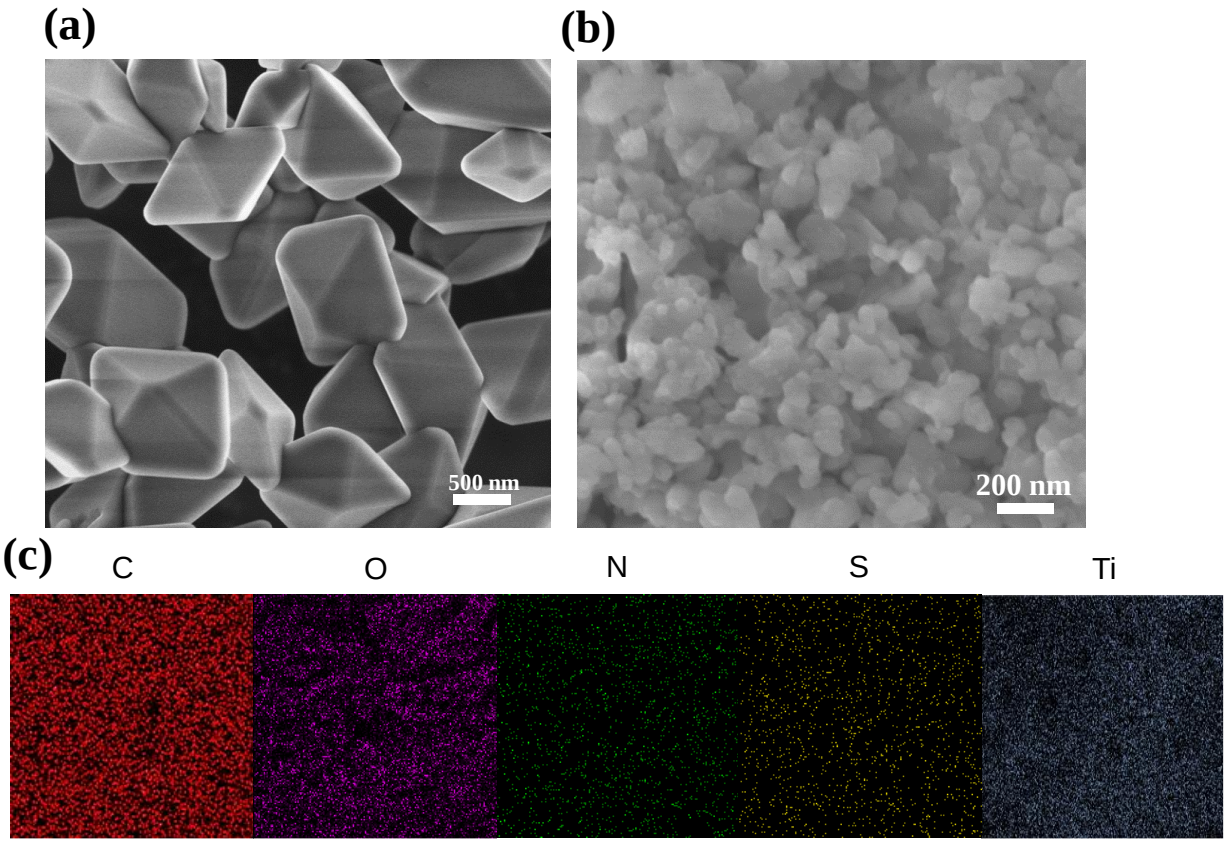

Figure S8. (a) SEM image of TiO_2 in SN-MQDs, (b) SEM image of sulfur and nitrogen doped Ti_3C_2 and corresponding SEM-EDS (energy dispersive spectrometer) elemental mapping images.

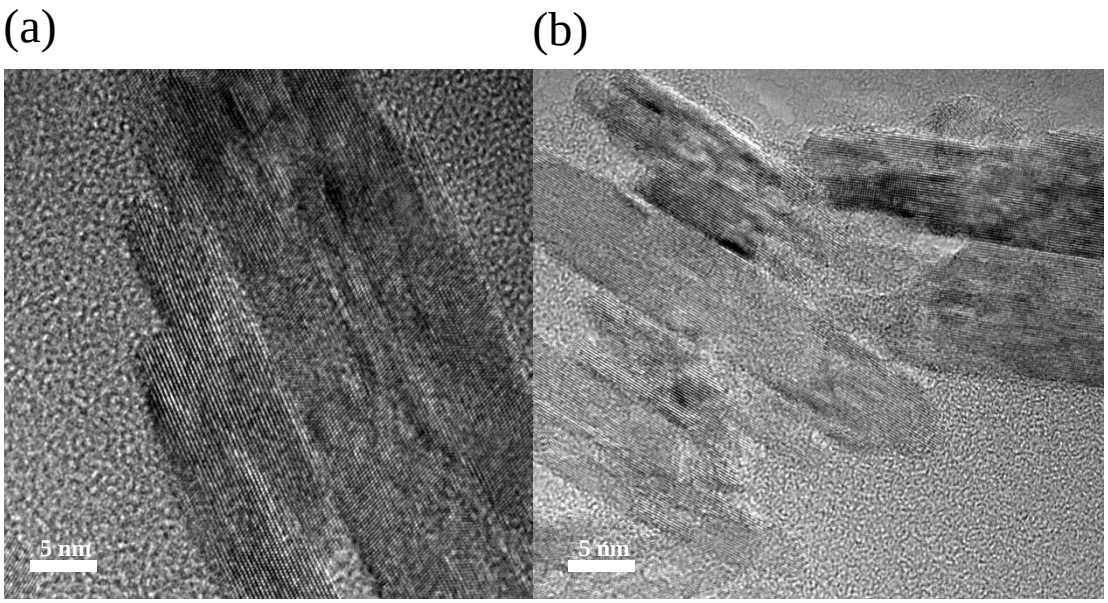

Figure S9. (a) HRTEM images of Ti_3C_2 (a) before and (b) after acid treatment.

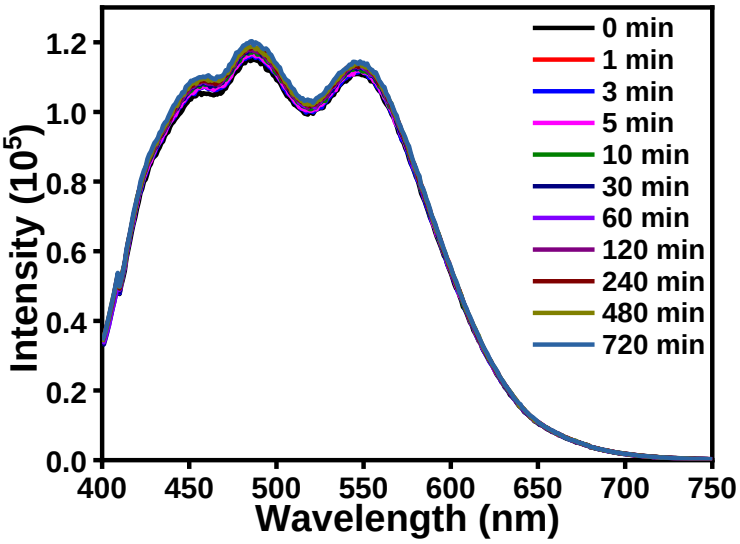

Figure S10. Time-dependent fluorescence spectra of W-MQDs under 360 nm emission.

Table S1. The quantum yields up of the as-prepared SN-MQDs and other materials.

Samples	QY (%)	Ref.
SN-MQDs	28.12	This paper
Ti_3C_2 QDs	18.7	[47]
Ti_3C_2 QDs	10	[39]
Ti_3C_2 QDs	7.13	[56]
MoS_2 QDs	4.4	[43]
g-C_3N_4 QDs		[44]

Table S2. Photoluminescence quantum yield (%) of the as-synthesized MQDs by the hydrothermal method and redispersed in water and alcohol.

Samples	QY (%)	Samples	QY (%)	Samples	QY (%)	Samples	QY (%)
SN-MQDs	28.12	SN-MQDs (dry)	3.84	SN-MQDs (water)	24.32	SN-MQDs (alcohol)	4.72
N-MQDs	8.33	N-MQDs (dry)	5.35	N-MQDs (water）	8.15	N-MQDs (alcohol)	5.23
S-MQDs	7.78	S-MQDs (dry)	4.21	S-MQDs (water)	7.12		

Table S3. PL lifetimes (τ) of the as-synthesized MQDs by the hydrothermal method and redispersed in water and alcohol.

Samples	τ_1 (ns)	A_1 (%)	τ_2 (ns)	A_2 (%)	τ_3 (ns)	A_3 (%)	χ^2	τ (ns)
S-MQDs	1.93	76.7341	7.13	23.2659			1.072	4.677071
S-MQDs (dry)	0.74	72.7566	2.49	24.6119	8.86	2.6315	1.053	2.882202
S-MQDs (water)	2.11	56.5705	7.14	43.4295			1.128	5.741934
N-MQDs	2.13	66.3865	7.79	33.6135			1.070	5.808949
N-MQDs (dry)	0.82	61.1115	2.87	34.1848	10.41	4.7037	1.001	4.22136
N-MQDs (water)	1.97	70.5125	7.22	29.4875			1.062	5.147071
N-MQDs (alcohol)	1.63	83.2269	7.32	16.7731			1.019	4.333199
SN-MQDs	2.80	25.0562	8.31	74.9438			1.072	7.746613
SN-MQDs (dry)	0.74	71.337	2.55	25.337	7.97	3.326	1.038	2.884418
SN-MQDs (water)	2.63	37.7016	8.79	62.2984			1.035	7.845605
SN-MQDs (alcohol)	1.44	86.9923	6.92	13.0077			1.108	3.731289